Contents

Chapter 1

Introduction

1.1 Forms of carbon material

Carbon material world has four main classes in dimension: diamond and graphite (3D), graphene - one layer of graphite (2D), carbon nanotube (CNT) (1D), and fullerene (0D)(See Fig. 1.1). The latter two forms of carbon were recently discovered and opened a new page of carbon material. Fullerene was discovered in 1985 by Robert F. Curl, Sir Horold W. Kroto, and Richard E. Smalley [1], and awarded Nobel prize in chemistry in 1996. In 1993, A narrow, tubular structure rolled up from graphene was discovered and named "carbon nanotube" [2, 3], which became a new member of the carbon family. Due to its nano-scale structure and prominent mechanical, thermal and electronic properties, CNT is becoming the most focused topic in nano-technology research.

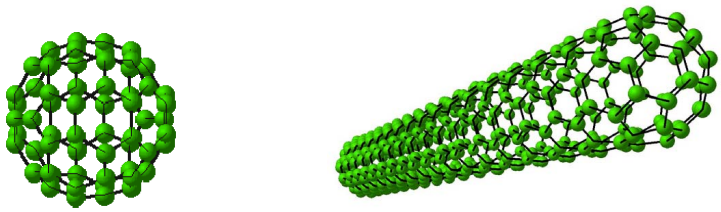

(a) C_{60} (b) SWNT

Figure 1.1: Two recently discovered forms of carbon, (a) C_{60} or the "buckyball", known as a quantum dot, and (b) a single-walled carbon nanotube, which can be imagined from elongating a buckyball or rolling up a graphene sheet.

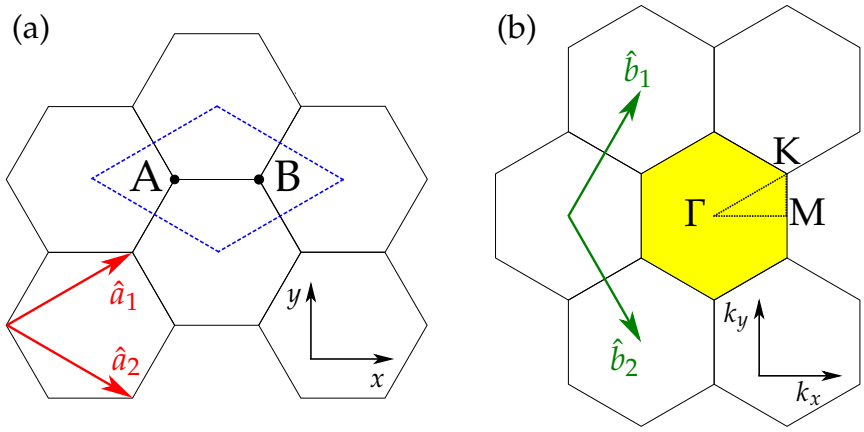

Figure 1.2: (a) The unit cell of graphene (enclosed by the dashed rhombus) contains two atoms A and B. (b) The Brillouin zone (yellow region), and high symmetry points M, K, and Γ. The real- and reciprocal-space unit vectors are shown by $\hat{a}_i$ and $\hat{b}_i$ ($i = 1, 2$).

1.2 SWNT fundamentals

A carbon nanotube has nanometer scale in diameter but a length from μm to cm. This great aspect ratio makes it a quasi-one-dimensional material. CNTs can be divided into three types based on the number of walls as single-walled (SWNTs), concentric multi-walled (MWNTs), and double-walled carbon nanotubes (DWNTs).

SWNTs have many exceptional properties that arise from their unique structure. The diameter of a SWNT is small enough that quantum effects become significant, however the length of a SWNT is macroscopic in scale, making quantum effects negligible along the nanotube. This combination of length scales gives SWNTs some very interesting properties. Here, a formal description of SWNT structure is given, followed with the discussion on its electronic properties [4, 5, 6].

1.2.1 Geometry of SWNTs

Graphene has sp^2 hexagonal carbon network structure based on the unit cell shown in Fig. 1.2a. Two unit vectors $\hat{a}_1$ and $\hat{a}_2$ are used to describe the hexagonal lattice, and expressed in Cartesian coordinates as

$$\hat{a}_1 = \left(\frac{\sqrt{3}}{2}a,\ \frac{a}{2}\right) \qquad \hat{a}_2 = \left(\frac{\sqrt{3}}{2}a,\ -\frac{a}{2}\right), \tag{1.1}$$

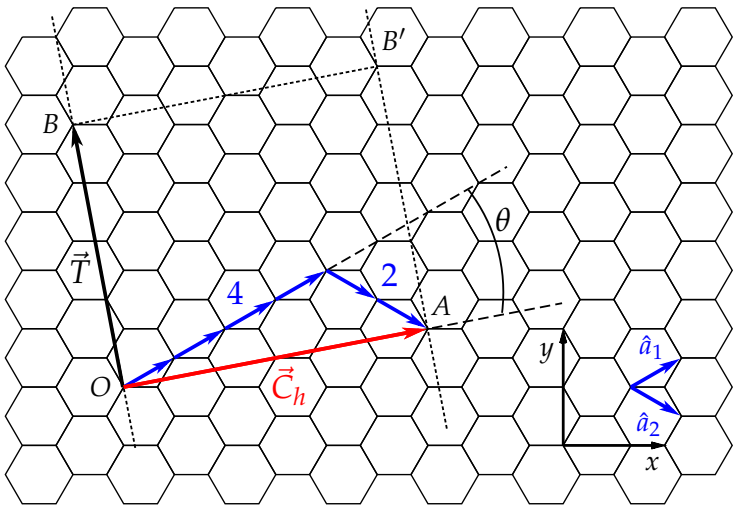

Figure 1.3: The chiral vector $\vec{C}_h$ for an (n, m) = (4,2) SWNT. The chiral angle is shown by θ.

where $|\hat{a}_1| = |\hat{a}_2| = a = \sqrt{3}a_{cc}$, where a_{cc} = 1.42 Å is the distance between neighboring carbon atoms. The first Brillouin zone (BZ) of graphene is shown in Fig. 1.2b. This is the momentum space reciprocal lattice, and is spanned by the reciprocal space basis vectors $\hat{b}_1$ and $\hat{b}_2$, which are defined as

$$\hat{b}_1 = \left(\frac{2\pi}{\sqrt{3}a}, \frac{2\pi}{a}\right) \qquad \hat{b}_2 = \left(\frac{2\pi}{\sqrt{3}a}, -\frac{2\pi}{a}\right). \tag{1.2}$$

The structure of carbon nanotube is specified by the chiral vector C_h as shown in Fig. 1.3, which defines the direction of rolling up the graphene sheet into a tube (point A and B′ is overlapped with point O and B, respectively). Chiral vector C_h can be expressed in terms of the real space unit vectors as $n\hat{a}_1 + m\hat{a}_2 \equiv (n, m)$, where n and m are positive integers, and $n \geq m$. The angle θ that $\vec{C}_\mathrm{h}$ makes with $\hat{a}_1$ is called the chiral angle, and for symmetry reasons $0 \leq \theta \leq \pi/6$. The diameter of the SWNT, $d_t = |\vec{C}_h| = a\sqrt{n^2 + m^2 + nm}$. The vector $\vec{T}$ in Fig. 1.2 is called the translation vector, and is the 1D unit vector of the SWNT. It is oriented parallel to the SWNT axis, and perpendicular to $\vec{C}_h$. The translation vector is defined as $\vec{T} = t_1\hat{a}_1 + t_2\hat{a}_2 \equiv (t_1, t_2)$, where

$$t_1 = \frac{2m + n}{d_R} \qquad t_2 = -\frac{2n + m}{d_R}. \tag{1.3}$$

The value d_R in equation (1.3) is the greatest common divisor (gcd) of $(2m + n)$ and $(2n + m)$.

By Euclid's law, it turns out that

$$d_R = \begin{cases} d & \text{if } n-m \text{ is not a multiple of 3d} \\ 3d & \text{if } n-m \text{ is a multiple of 3d} \end{cases}, \tag{1.4}$$

where $d = gcd(n, m)$. The vectors $\vec{C}_h$ and $\vec{T}$ define the rectangle $OAB'B$ in Fig. 1.3, which encloses the unit cell of the SWNT. The number of hexagons in the unit cell is N, where

$$N = \frac{|\vec{C}_h \times \vec{T}|}{|\hat{a}_1 \times \hat{a}_2|} = \frac{2(m^2 + n^2 + nm)}{d_R}. \tag{1.5}$$

The combinations of (n, m) give rise to many possible SWNT structures, which generally can be classified by chiral angle and described as achiral (zigzag and armchair) and chiral SWNT (See Fig. 1.4).

1.2.2 Electronic properties of SWNTs

The dimensions of the 3D bulk material are much larger than the constituent elements, which allows for a continuum of possible electronic state. But when going from a bulk material to a low dimensional material, the electronic states are constrained by quantum effects in the nanoscale direction, which can be considered as a subset of the electronic states of the bulk material. The electronic density of state (DOS) dependence on energy $g(E)$ is given by $g \propto (E - E_0^{(d/2-1)})$, where D denotes the dimension (see Fig. 1.5).

In SWNT, since the unit vectors are $\vec{C}_h$ and $\vec{T}$, the reciprocal lattice vectors corresponding to the circumferential direction $\vec{K}_1$ and the axial direction $\vec{K}_2$ are defined with the

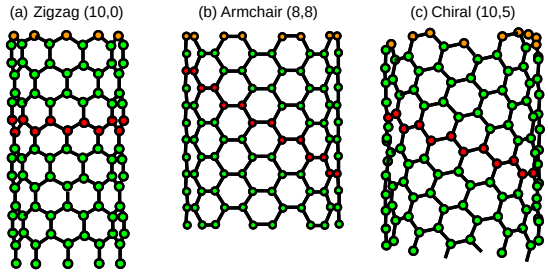

Figure 1.4: Examples of the three different SWNT geometries, zigzag, armchair, and chiral.

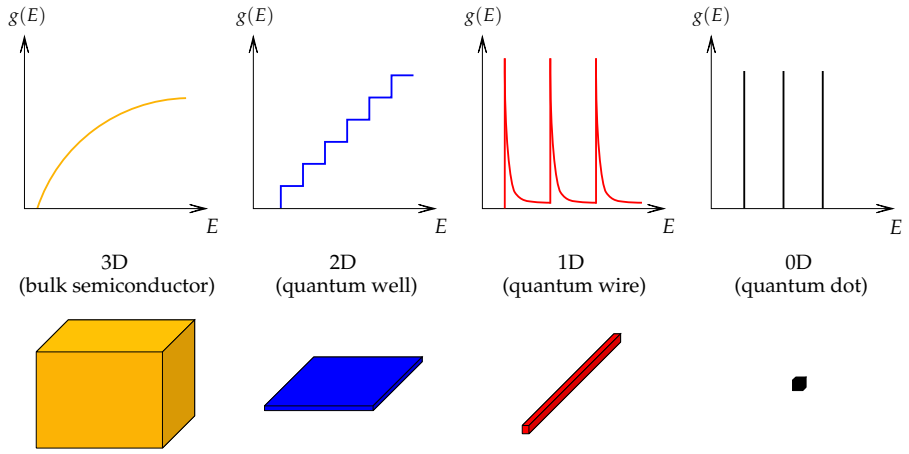

Figure 1.5: Typical density of states $g(E)$ for materials of different dimensionality. Quantum effects confine the allowed states as the dimensionality is reduced.

following relations,

$$\vec{C}_h \cdot \vec{K}_1 = \vec{T} \cdot \vec{K}_2 = 2\pi, \ \vec{C}_h \cdot \vec{K}_2 = \vec{T} \cdot \vec{K}_1 = 0. \tag{1.6}$$

Then obtains the expressions for $\vec{K}_1$ and $\vec{K}_2$

$$\vec{K}_1 = \frac{1}{N}(-t_2\vec{b}_1 + t_1\vec{b}_2)\vec{K}_2 = \frac{1}{N}(m\vec{b}_1 - n\vec{b}_2) \tag{1.7}$$

The first Brillouin zone of the SWNT is expressed as a segment of $\vec{K}_2$ noted as "cutting lines"(Fig. 1.6).

The method of constructing 1D electronic energy subbands by cutting the 2D electronic dispersion relations of graphene with these lines is known as the "zone-folding

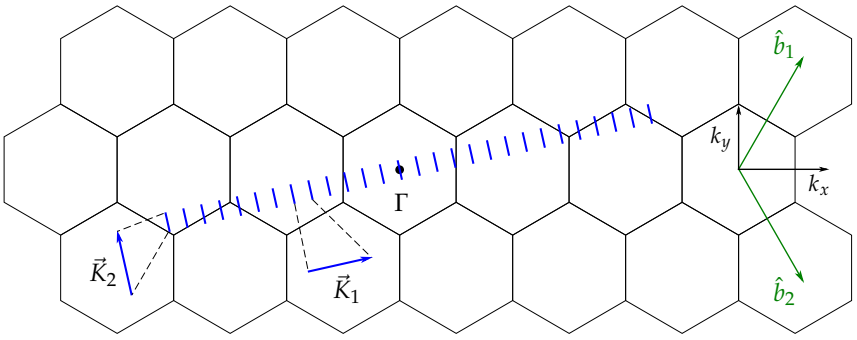

Figure 1.6: Cutting lines in the Brillouin zone for a (4,2) nanotube.

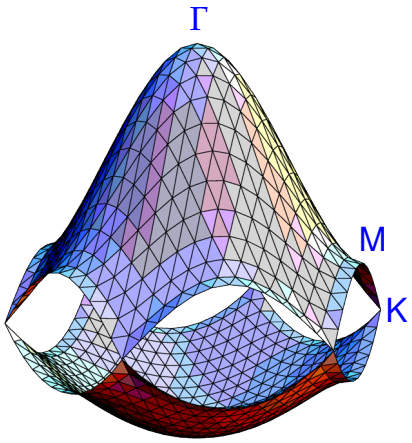

Figure 1.7: The electronic density of states (DOS) calculated over the entire Brillouin zone of graphene. The labels indicate high-symmetry points (Figure courtesy R. Saito, Tohoku University).

scheme" (Fig.1.7). The quantized wave vector of SWNTs causes a sharp divergence in their DOS, noted "van Hove singularities" as shown in Fig. 1.8.

If the cutting line does not pass the *K*-point in first BZ, the DOS is zero at the Fermi level, which makes it intrinsic semiconducting as the (4,2) SWNT shown in Fig.1.8. If it passes the *K*-point, the valence and conduction bands will touch each other, and give rise to a nonzero value of DOS at Fermi level, which makes it metallic as the (5,5) SWNT.

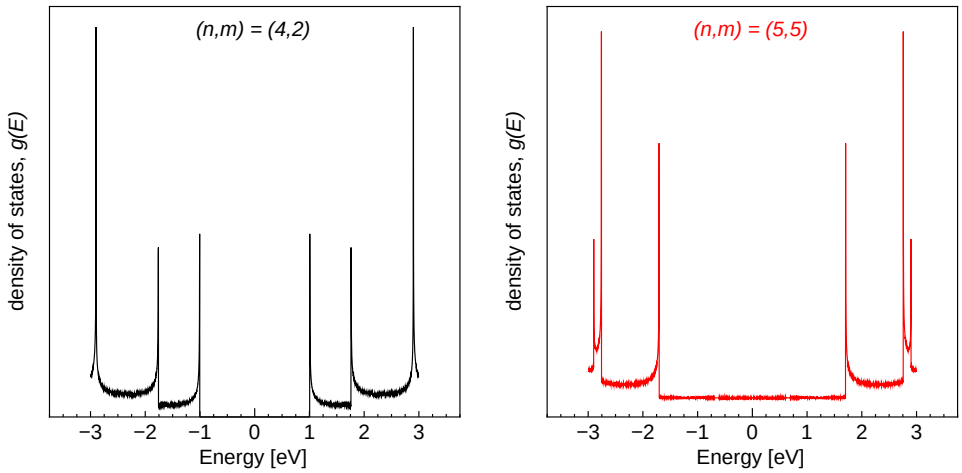

Figure 1.8: Plots of the density of states for a semiconducting (4,2) chiral SWNT, and a metallic (5,5) armchair SWNT

Hence, the electronic property of a SWNT is inherently determined by (n,m). In general, if $mod(n-m)=0$, the SWNT is metallic, otherwise, it is semiconducting. Thus, statistically speaking, one thirds SWNTs are metallic, and two thirds are semiconduciting.

1.3 Raman spectroscopy

1.3.1 Raman scattering

When light is scattered from a molecule or a solid material, most photons are elastically scattered, which means no energy difference between incident and scattered light, and it is called Rayleigh scattering. However, a small fraction of light (approximately $1/10^7$) is inelastically scattered, with a frequency different from incident photons, which is called Raman scattering. In resonant Raman scattering, three processes occur as shown in Fig. 1.9: (1) an electron is excited from the valence energy band to the conduction energy band by absorbing a photon, (2) the excited electron is scattered by emitting (absorbing) phonons, and (3) the electron relaxes to the valence band by emitting a photon. If the scattered photon has lower frequency than incident photon (losing energy to phonons), it is called Stokes Raman scattering; if it has higher frequency (gaining energy from phonons), it is called anti-Stokes Raman scattering.

By plotting the intensity of scattered light as a function of energy difference noted

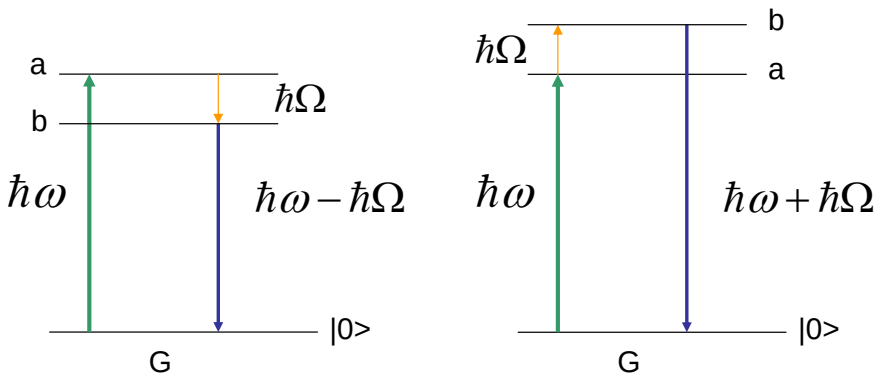

Figure 1.9: Raman processes of (a) Stokes-scattering, (b) anti-Stokes-scattering.

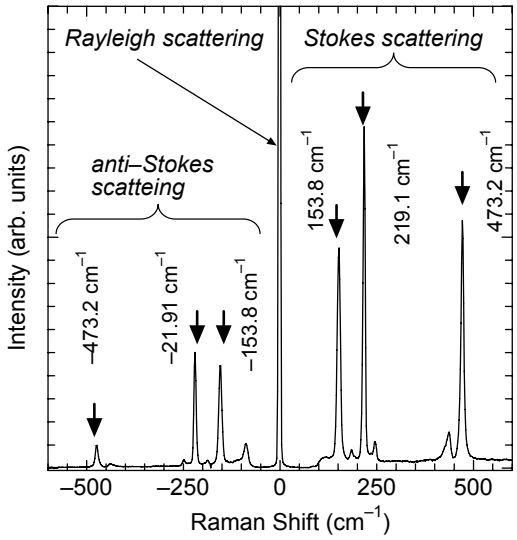

Figure 1.10: Raman spectroscopy with Stokes and anti-Stokes signals take from Sulfur (from [7])

as "Raman shift"(in unit cm^{-1}), we obtain Raman spectroscopy (Fig.1.10). The Stokes and anti-Stokes scattering signals are symmetric to the Rayleigh scattering (Raman shift=0) in Raman spectroscopy, since they all indicate the same phonon energy of the material. Raman intensity is proportional to the number of phonons, which can be described by Boltzmann distribution, therefore we obtain more intense signals in Stokes Raman scattering and usually only plot them in Raman spectra. Usually Raman spectra reveal phonon explicitly, being independent of the electronic structure of materials and excitation laser energy, and in weak intensity. However, the scattering efficiency is largely enhanced when incident (scattered) photon matches the energy separation between two electronic states (see Fig. 1.11(a) and (b)), and this process is called resonance Raman spectroscopy (RRS). It becomes a widely-used technique to improve the S/N ratio in Raman spectra.

1.3.2 Raman spectroscopy of SWNTs

The resonance Raman spectroscopy is a widely used in characterizing SWNTs not only because it is a non-contact and non-destructive measurement, but also it can provides abundant information such as electronic energy structure, electronic type (semiconducting or metallic), diameter distribution from the resonance conditions and Raman signals.

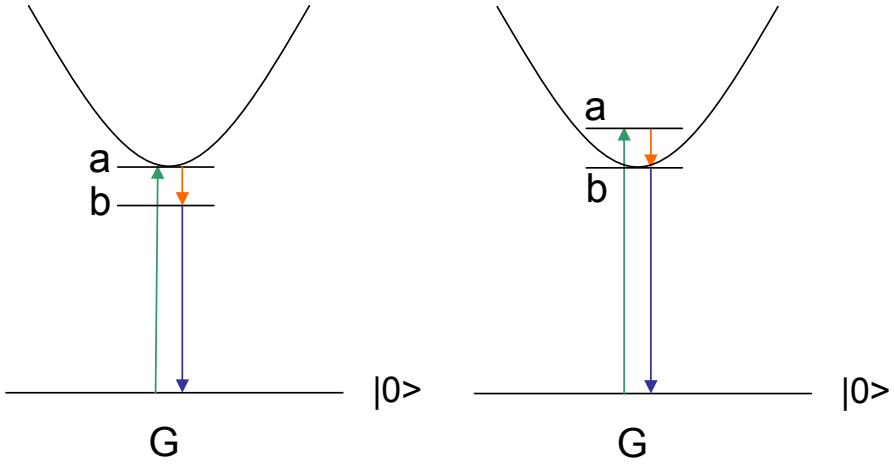

(a) (b)

Figure 1.11: First-order resonance Raman processes, (a) incident resonance process and (b) scattered resonance process. G, a and b denote, respectively, the ground state and the intermediate states.

Here, three important features in Raman spectroscopy from SWNTs, RBM (Radial Breathing Mode), G-band, and D-band, are introduced.

1.3.2.1 Electronic structures and Kataura plot

CNTs are one-dimensional (1D) system which has specific electronic energy structures determined by von Hove singularities (vHSs) in the density of electronic states (DOS). Each nanotube has its unique DOS determined by chirality and distinct electron and phonon structure. Only when the electronic energy separations between vHSs in the valence and conduction bands equals to laser energy, the resonant Raman signal can be observed, but restricted to the selection rules of optical transition. Therefore in the Raman spectra of bundled CNTs, signals are strongly contributed by those in resonance with the excitation laser energy. The plot of optically allowed transition energy (E_{ii}) versus nanotube diameter (d_t), called "Kataura plot"(Fig.1.12), are useful when considering resonance conditions of CNTs. It can be used for estimating possible CNTs appearing in RRS and therefore choosing a excitation laser.

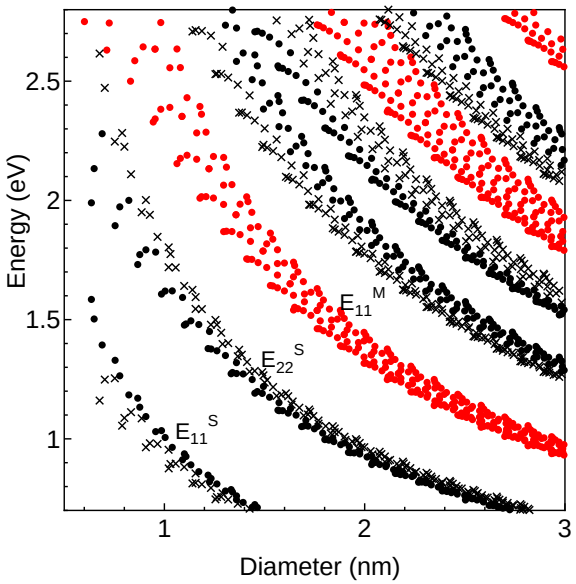

Figure 1.12: Kataura plot calculated by tight-binding theory from [8]

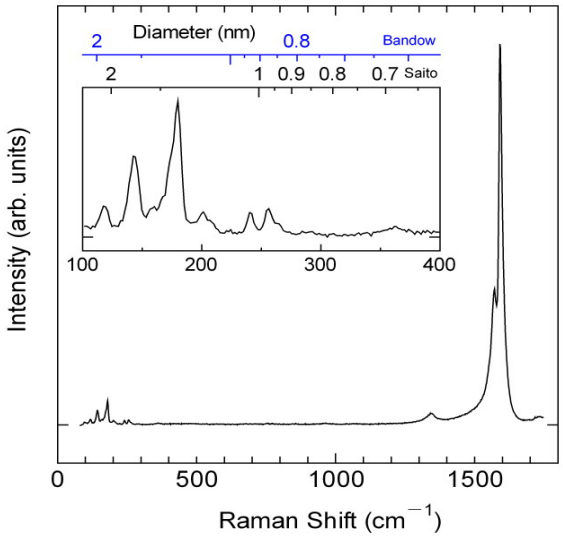

Figure 1.13: A typical Raman spectroscopy from VA-SWNTs (488 excitation laser). The RBM peaks are shown in the insert.

1.3.2.2 Radial breathing modes-RBM

The RBM feature is a totally symmetric vibration mode appearing at around 100 to 400 cm^{-1} as shown in Fig.1.13, which corresponds to the carbon atoms vibration in the

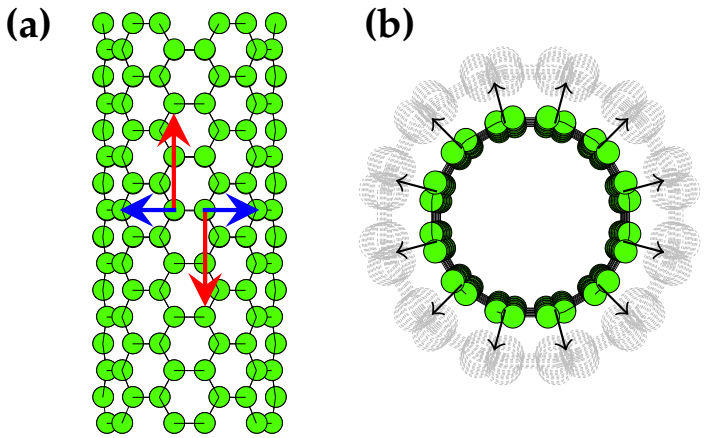

Figure 1.14: (a) the in-plane vibration modes corresponding to the G-band Raman signal, and (b)the uniform out-of-plane vibration that gives rise to RBM Raman signal

radial direction as if the tube was breathing (Fig. 1.14). It is very useful in characterizing the nanotube diameters by the relation of $\omega_{RBM} = \frac{A}{d_t} + B$. The sets of parameter A and B are assigned differently in each experimental data: $(A = 248, B = 0)$ for CNTs on a SiO_2 substrate; $(A = 239, B = 0)$ for bundled CNTs, $(A = 218, B = 16)$ for CNTs dispersed in aqueous solution, and $(A = 204, B = 27)$ for free-standing CNTs [9]. The simple force constance calculations predict a linear relation between ω_{RBM} and d_t. However, when considering small diameter CNTs samples it converges to

$$\omega_{RBM} = \frac{219 \pm 3}{d_t} + (15 \mp 3)$$

which fits the VA-SWNTs sample very well [10]. By combining the information of diameter and the resonant transition energy ($E_{ii} = E_L$) in Kataura plot,we can easily assign tube chiralities corresponding to each RBM peak. Since in each Raman spectrum, only the CNTs in resonance will contribute to the signals, it is limited to indicate CNT diameter distribution by only one laser excitation. By using many laser excitations, we can obtain a much more accurate composition of CNTs from the RRS profile[10].

1.3.2.3 Tangential modes G-band

In graphite, a peak at $1582\,\mathrm{cm}^{-1}$ is called G-mode, which indicates the in-plane tangential optical phonon. Due to the curvature effect in CNTs, the G-mode gives rise to

multi-peak features, so called G-band, where up to six peaks can be observed. The two most intense G peaks at 1590 and 1570 cm^{-1} are labelled G^+ and G^-, which are associated, respectively, to the vibration of carbon atoms along the tube axis (LO phonon) and along the circumferential direction (TO phonon) for semiconducting SWNTs (Fig. 1.14). The shape of G^- peak is broadened for the metallic CNTs due to the electron-phonon interaction, which gives a Breit-Winger-Fano (BWF) lineshape

$$I(\omega) = I_0 \frac{[1 + (\omega - \omega_{BWF})/q\Gamma]^2}{1 + [(\omega - \omega_{BWF})/\Gamma]^2}.$$

The G^- peak also shows a diameter dependence which is not found with G^+. The frequency difference of these G^+ and G^- can be fitted very well with the function of $\omega_{G^-} = \omega_{G^+} - C/d_t^2$, with $\omega_{G^+} = 1591\,cm^{-1}$ and $C = 47.7(79.5)\,cm^{-1}$ for semiconducting (metallic) CNTs. Moreover, according to the group theory and selection rules, polarization study of six phonon mode can be observed from G-band peaks [11][12].

1.3.2.4 Disorder-induced D-band

The D-band at 1300-1400 cm^{-1} is a second order Raman scattering feature, which is related to the defects in the CNTs (impurities or missing atoms, finite-size effects and molecules linked to the nanotube sidewalls) or the presence of amorphous carbon material [9]. As the metric for the internal calibration procedure, the I_D/I_G intensity ratio is used to identify the defect in CNTs. The more defect in material, the broader D band, and the larger I_D/I_G ratio. But this analysis should also considers resonance condition, for observation of large D band in isolated SWNT usually means a bad resonance condition [13]. The D band frequency is dependent on the excitation laser energy E_L both in isolated and bundled CNTs [9].

Chapter 2

Selection Rules for Raman Scattering Process

2.1 Geometry of Raman observation

The geometry of Raman observation is usually expressed by four vectors

$$\boldsymbol{P}_g[\boldsymbol{P}_i, \boldsymbol{P}_s]\boldsymbol{P}_o \quad (\boldsymbol{P} = \boldsymbol{X}, \boldsymbol{Y}, \boldsymbol{Z})$$

where $\boldsymbol{P}_g$ and $\boldsymbol{P}_o$ are, respectively, the propagating directions of incident light and scattered light, and $\boldsymbol{P}_i$ and $\boldsymbol{P}_s$ are polarization directions of the electric field of the incident and scattered light. We put a SWNT in the direction of z-axis. We usually observe the signal propagating along y-axis and backscattered, therefore the geometry is $\boldsymbol{Y}[\boldsymbol{P}_i, \boldsymbol{P}_s]\bar{\boldsymbol{Y}}$. By changing the polarization of light relative to the tube axis, we can select specific symmetry allowed phonon modes [14].

2.2 Selection rules for optical transitions

By using dipole approximation for optical transitions, the corresponding dipole selection rule describes the allowed transition between sub-bands of the valence and conduction bands as $E^v_\mu \rightarrow E^c_{\mu'}$ $(\mu' = \mu)$ for the light polarized along tube axis and as $E^v_\mu \rightarrow E^c_{\mu'}$ $(\mu' = \mu \pm 1)$ for the light polarized perpendicular to the tube axis [4, 15, 16].

2.3 Electron phonon interaction

In electron phonon interaction, phonons can scatter electrons from one cutting line μ to another cutting line μ', depending on the phonon symmetry, but subject to $\Delta\mu = \mu - \mu'$ (angular momentum conservation). A phonon mode does not change cutting line ($\Delta\mu = 0$), while in E_j phonon modes we have $\Delta\mu = \pm j$. Combining the electron-incident photon, electron-phonon, electron-scattered photon interactions, yields the following possible Raman process in SWNTs [17, 12]:

$$\begin{aligned}
&E_\mu^v \xrightarrow{\parallel} E_\mu^c \xrightarrow{A(\boldsymbol{ZZ})} E_\mu^c \xrightarrow{\parallel} E_\mu^v \\
&E_\mu^v \xrightarrow{\perp} E_{\mu\pm1}^c \xrightarrow{A(\boldsymbol{XX})} E_{\mu\pm1}^c \xrightarrow{\perp} E_\mu^v \\
&E_\mu^v \xrightarrow{\parallel} E_\mu^c \xrightarrow{E_1(\boldsymbol{ZX})} E_{\mu\pm1}^c \xrightarrow{\perp} E_\mu^v \\
&E_\mu^v \xrightarrow{\perp} E_{\mu\pm1}^c \xrightarrow{E_1(\boldsymbol{XZ})} E_\mu^c \xrightarrow{\parallel} E_\mu^v \\
&E_\mu^v \xrightarrow{\perp} E_{\mu\pm1}^c \xrightarrow{E_2(\boldsymbol{XX})} E_{\mu\mp1}^c \xrightarrow{\perp} E_\mu^v
\end{aligned} \tag{2.1}$$

From above, we know that A mode can be observed for $E_{\mu\mu}$ excitation in ($\boldsymbol{ZZ}$) geometry or $E_{\mu,\mu\pm1}$ excitation in ($\boldsymbol{XX}$) geometry. E_1 mode can be observed for $E_{\mu\mu}$ excitation in ($\boldsymbol{ZX}$) geometry, or $E_{\mu,\mu\pm1}$ excitation in ($\boldsymbol{XZ}$) geometry. E_2 mode can be observed for $E_{\mu,\mu\pm1}$ excitation in ($\boldsymbol{XX}$) geometry.

2.4 Formulations for multiple dipole absorption by SWNTs

We assume that VA-SWNTs have 3-dimensional orientational distribution described by the following model [18]. The $x-y-z$ orthogonal coordinate is defined in which z-axis is normal to the substrate. Orientation of SWNT axis is defined by two angles $\varphi(0 \le \varphi \le \frac{\pi}{2})$ which is the angle between tube axis and z-axis, and $\gamma(0 \le \gamma \le 2\pi)$ which is the rotational angle of a plane constructed by tube axis and z-axis. Selection rules allow two dipoles in first-order Raman scattering process of SWNTs, which are dipole $\boldsymbol{\mu}_{\shortparallel}$ parallel to the tube axis, and dipole $\boldsymbol{\mu}_{\perp}$ perpendicular to the tube axis. The parallel dipole $\boldsymbol{\mu}_{\shortparallel}$ can be expressed as

$$\boldsymbol{\mu}_{\shortparallel} = \mu_{\shortparallel} \begin{pmatrix} \sin\varphi\cos\gamma \\ \sin\varphi\sin\gamma \\ \cos\varphi \end{pmatrix}. \tag{2.2}$$

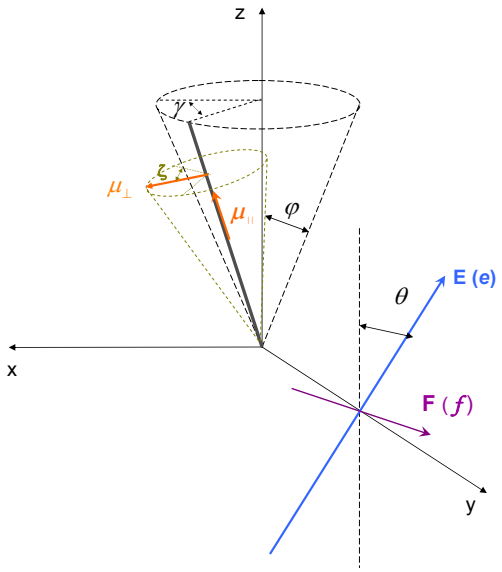

Figure 2.1: scheme of 3-dimensional distributed SWNTs and dipole assumption

Since $\boldsymbol{\mu}_\perp$ has all the components around ζ, the dipole at specific angle ζ is given by

$$\boldsymbol{\mu}_\perp = \boldsymbol{\mu}_{\perp(\zeta=0)} \cos\zeta + \boldsymbol{\mu}_{\perp(\zeta=\frac{\pi}{2})} \sin\zeta \tag{2.3}$$

in which vector $\boldsymbol{\mu}_{\perp(\zeta=0)}$ and $\boldsymbol{\mu}_{\perp(\zeta=\pi/2)}$ are expressed as

$$\boldsymbol{\mu}_{\perp(\zeta=0)} = \mu_\perp \begin{pmatrix} -\sin\gamma \\ \cos\gamma \\ 0 \end{pmatrix}, \qquad \boldsymbol{\mu}_{\perp(\zeta=\frac{\pi}{2})} = \mu_\perp \begin{pmatrix} -\cos\varphi\cos\gamma \\ -\cos\varphi\sin\gamma \\ \sin\varphi \end{pmatrix}. \tag{2.4}$$

Substituting equation 2.4 to 2.3 we can obtain the expression for $\boldsymbol{\mu}_\perp$ as

$$\boldsymbol{\mu}_\perp = \boldsymbol{\mu}_{\perp(\zeta=0)} \cos\zeta + \boldsymbol{\mu}_{\perp(\zeta=\frac{\pi}{2})} \sin\zeta = \mu_\perp \begin{pmatrix} -\sin\gamma\cos\zeta - \cos\varphi\cos\gamma\sin\zeta \\ \cos\gamma\cos\zeta - \cos\varphi\sin\gamma\sin\zeta \\ \sin\varphi\sin\zeta \end{pmatrix}. \tag{2.5}$$

The electric field unit vector of incident photon $\boldsymbol{E}$ is given by

$$\boldsymbol{E} = \begin{pmatrix} -\sin\theta \\ 0 \\ \cos\theta \end{pmatrix}, \tag{2.6}$$

where θ is the angle between electric field vector and z-axis. In the experiments, two configurations are utilized where the orientation of polarizer for inspecting scattered photon

is parallel to(VV) or perpendicular to (VH) the incident light polarization. In VH configuration, the polarizer orientation vector is described by

$$\boldsymbol{f} = \begin{pmatrix} -\cos\theta \\ 0 \\ -\sin\theta \end{pmatrix}. \tag{2.7}$$

2.4.1 Dipole approximation for absorption process

First we consider the case of only one SWNT. The absorption probability is proportional to the square of the inner product of electric filed vector and allowed dipole vector. If it absorbs light parallel to the tube axis, the absorption probability is represented as

$$I_{\shortparallel}(\gamma, \varphi, \theta) \propto I_{ex}|\boldsymbol{E} \cdot \boldsymbol{\mu}_{\shortparallel}|^2 \tag{2.8}$$

where I_{ex} is the intensity of incident light. If it absorbs light perpendicular to the tube axis, the absorption probability is

$$I_{\perp}(\gamma, \varphi, \theta) \propto I_{ex} \int_0^{2\pi} |\boldsymbol{E} \cdot \boldsymbol{\mu}_{\perp}|^2 d\zeta \tag{2.9}$$

Next we consider the case SWNTs distributed in three dimensions. We assume that SWNTs are uniformly distributed around z-axis, thus they have a distribution function $\rho(\varphi)$ with only one variable φ. Applying distribution function $\rho(\varphi)$, we obtain the expression for integrity of equation 2.8 as

$$\begin{aligned} I_{\shortparallel}(\theta) &\propto \int_0^{\frac{\pi}{2}} \int_0^{2\pi} I_{ex}|\boldsymbol{E} \cdot \boldsymbol{\mu}_{\shortparallel}|^2 \rho(\varphi)\, d\gamma d\varphi \\ &\propto I_{ex}\mu_{\shortparallel}^2 \int_0^{\frac{\pi}{2}} \int_0^{2\pi} (-\sin\theta \sin\varphi \cos\gamma + \cos\theta \cos\varphi)^2 \rho(\varphi)\, d\gamma d\varphi \\ &\propto I_{ex}\mu_{\shortparallel}^2 \int_0^{\frac{\pi}{2}} \int_0^{2\pi} (\sin^2\theta \sin^2\varphi \cos^2\gamma + \cos^2\theta \cos^2\varphi \\ &\quad - 2\sin\theta \cos\theta \sin\varphi \cos\varphi \cos\gamma) \rho(\varphi) d\gamma d\varphi. \end{aligned}$$

Noting that

$$\int_0^{2\pi} \cos\gamma d\gamma = 0 \qquad\qquad \int_0^{2\pi} \cos\gamma^2 d\gamma = \pi$$

we obtain

$$I_{\shortparallel}(\theta) \propto \Lambda_{\shortparallel}(\frac{1}{2}\sin^2\theta \left\langle \sin^2\varphi \right\rangle + \cos^2\theta \left\langle \cos^2\varphi \right\rangle) \tag{2.10}$$

where $\Lambda_{\shortparallel} = I_{ex}\ \mu_{\shortparallel}^2$ and $\langle f(\varphi)\rangle = \int_0^{\frac{\pi}{2}} f(\varphi)\rho(\varphi)d\varphi$.

Similarly, we can obtain the expression of $I_{\perp}(\theta)$ by applying the three-dimensional distribution $\rho(\varphi)$ as

$$\begin{aligned} I_{\perp}(\theta) &\propto \int_0^{\frac{\pi}{2}} \int_0^{2\pi} I_{ex} \int_0^{2\pi} |\boldsymbol{E}\cdot\boldsymbol{\mu}_{\perp}|^2 d\zeta d\gamma d\varphi \\ &\propto \Lambda_{\perp}(1-(\frac{1}{2}\sin^2\theta\left\langle\sin^2\varphi\right\rangle + \cos^2\theta\left\langle\cos^2\varphi\right\rangle)) \end{aligned} \tag{2.11}$$

where $\Lambda_{\perp} = I_{ex}\ \frac{1}{2}\mu_{\perp}^2$.

Therefore, the following relations can be deduced

$$\begin{aligned} I_{\shortparallel}(0) &= \Lambda_{\shortparallel}\left\langle\cos^2\varphi\right\rangle \\ I_{\perp}(0) &= \Lambda_{\perp}(1-\left\langle\cos^2\varphi\right\rangle) \\ I_{\shortparallel}(\frac{\pi}{2}) &= \Lambda_{\shortparallel}\frac{1}{2}\left\langle\sin^2\varphi\right\rangle \\ I_{\perp}(\frac{\pi}{2}) &= \Lambda_{\perp}(1-\frac{1}{2}\left\langle\sin^2\varphi\right\rangle). \end{aligned}$$

Experimentally, we use the incident light with $\theta = 0$ and $\theta = \frac{\pi}{2}$ to get the optical absorption spectra of VA-SWNTs, in which

$$I_{exp}(0) = \Lambda_{\shortparallel}\left\langle\cos^2\varphi\right\rangle + \Lambda_{\perp}(1-\left\langle\cos^2\varphi\right\rangle) \tag{2.12}$$

$$I_{exp}(\frac{\pi}{2}) = \Lambda_{\shortparallel}\frac{1}{2}\left\langle\sin^2\varphi\right\rangle + \Lambda_{\perp}(1-\frac{1}{2}\left\langle\sin^2\varphi\right\rangle). \tag{2.13}$$

Combining the equation 2.12 and 2.13, the following relation can be deduced

$$\frac{I_{exp}(0)-I_{exp}(\frac{\pi}{2})}{I_{exp}(0)+2_{exp}I(\frac{\pi}{2})} = \frac{\Lambda_{\shortparallel}-\Lambda_{\perp}}{\Lambda_{\shortparallel}+2\Lambda_{\perp}}(\frac{3\left\langle\cos^2\varphi-1\right\rangle}{2}) = \frac{\Lambda_{\shortparallel}-\Lambda_{\perp}}{\Lambda_{\shortparallel}+2\Lambda_{\perp}}\cdot S, \tag{2.14}$$

where $S = (\frac{3\left\langle\cos^2\varphi-1\right\rangle}{2})$ is called nematic order parameter which indicates the alignment of a sample [19]. Therefore, if knowing the parameter $\mu_{\shortparallel}$ ($\Lambda_{\shortparallel}$) and $\mu_{\perp}$ ($\Lambda_{\perp}$), the alignment can be estimated from optical absorption.

2.4.2 Multi-dipole approximation for Raman process

Raman process can be simplified as two absorption process, since scattering can be seen as a reversed absorption. Here we use multi-dipole approximation for absorption and scattering process respectively to calculate the possibility of scattering light.

In polarized Raman measurement, we adopted two configurations for incident light and scattering observation noted as VV and VH. VV means polarization of incident light is parallel to the observation direction for scattered light (the direction of vector $\boldsymbol{E}$), while VH means they are perpendicular to each other (the direction of vector $\boldsymbol{E}$ and $\boldsymbol{f}$, respectively).

In VV configuration, we first consider the case of only one SWNT. If SWNT is excited by parallel incident photon and scatters photon parallel to the tube axis, the observed scattered photon intensity is noted as

$$I_{VV}^{\parallel\parallel} \propto I_{ex}|\boldsymbol{E}\cdot\boldsymbol{\mu}_{\shortparallel}|^2\, I_{em}|\boldsymbol{\mu}_{\shortparallel}\cdot\boldsymbol{E}|^2, \tag{2.15}$$

where I_{ex} and I_{ex} are intensity of incident and scattered photon. In $I_{VV}^{\parallel\parallel}$, "$\parallel\parallel$" denotes selection rule-allowed incident and scattered photon dipoles, and "VV" means experiment configuration.

Next we consider the case SWNTs distributed in three dimensions, and obtain the expression for integrity of scattered photon as

$$\begin{aligned}
I_{VV}^{\parallel\parallel} &\propto \int_0^{\frac{\pi}{2}}\int_0^{2\pi} I_{ex}|\boldsymbol{E}\cdot\boldsymbol{\mu}_{\shortparallel}|^2\, I_{em}|\boldsymbol{\mu}_{\shortparallel}\cdot\boldsymbol{E}|^2\rho(\varphi)\, d\gamma d\varphi \\
&\propto \int_0^{\frac{\pi}{2}}\int_0^{2\pi} (-\sin\theta\sin\varphi\cos\gamma+\cos\theta\cos\varphi)^4\rho(\varphi)\, d\gamma d\varphi \\
&\propto \int_0^{\frac{\pi}{2}}\int_0^{2\pi} (\sin^4\theta\sin^4\varphi\cos^4\gamma+\cos^4\theta\cos^4\varphi \\
&\quad +6\sin^2\theta\cos^2\theta\sin^2\varphi\cos^2\varphi\cos^2\gamma-4\sin\theta\cos^3\theta\sin\varphi\cos^3\varphi\cos\gamma \\
&\quad -4\sin^3\theta\cos\theta\sin^3\varphi\cos\varphi\cos^3\gamma)\rho(\varphi)\, d\gamma d\varphi.
\end{aligned}$$

Noting that

$$\int_0^{2\pi}\cos\gamma d\gamma = 0 \qquad \int_0^{2\pi}\cos\gamma^2 d\gamma = \pi$$
$$\int_0^{2\pi}\cos\gamma^3 d\gamma = 0 \qquad \int_0^{2\pi}\cos\gamma^4 d\gamma = \frac{3}{4}\pi,$$

we obtain

$$I_{VV}^{\parallel\parallel} \propto 2\cos^4\theta\left\langle\cos^4\varphi\right\rangle + 6\cos^2\theta\sin^2\theta\left\langle\sin^2\varphi\cos^2\varphi\right\rangle + \frac{3}{4}\sin^4\theta\left\langle\sin^4\varphi\right\rangle. \tag{2.16}$$

Following the method above, the other three possible cases $I_{VV}^{\parallel\perp}$, $I_{VV}^{\perp\parallel}$ and $I_{VV}^{\perp\perp}$ are

$$
\begin{aligned}
I_{VV}^{\parallel\perp} &\propto \int_0^{\frac{\pi}{2}} \int_0^{2\pi} \int_0^{2\pi} I_{ex} |\boldsymbol{E}\cdot\boldsymbol{\mu}_{\shortparallel}|^2 \, I_{em} |\boldsymbol{E}\cdot\boldsymbol{\mu}_{\perp}|^2 \rho(\varphi) \, d\zeta d\gamma d\varphi \\
&\propto \int_0^{\frac{\pi}{2}} \int_0^{2\pi} \int_0^{2\pi} |\boldsymbol{E}\cdot\boldsymbol{\mu}_{\shortparallel}|^2 \, |\boldsymbol{E}\cdot\boldsymbol{\mu}_{\perp}|^2 \rho(\varphi) \, d\zeta d\gamma d\varphi \\
&\propto 8\sin^2\theta\cos^2\theta - (3\sin^4\theta - 24\sin^2\theta\cos^2\theta + 8\cos^4\theta) \left\langle \sin^4\varphi \right\rangle \\
&\quad + 4(\sin^4\theta - 7\sin^2\theta\cos^2\theta + 2\cos^4\theta) \left\langle \sin^2\varphi \right\rangle
\end{aligned}
\tag{2.17}
$$

$$
\begin{aligned}
I_{VV}^{\perp\parallel} &\propto \int_0^{\frac{\pi}{2}} \int_0^{2\pi} \int_0^{2\pi} I_{ex} |\boldsymbol{E}\cdot\boldsymbol{\mu}_{\perp}|^2 \, I_{em} |\boldsymbol{E}\cdot\boldsymbol{\mu}_{\shortparallel}|^2 \rho(\varphi) \, d\zeta d\gamma d\varphi \\
&\propto \int_0^{\frac{\pi}{2}} \int_0^{2\pi} \int_0^{2\pi} |\boldsymbol{E}\cdot\boldsymbol{\mu}_{\perp}|^2 \, |\boldsymbol{E}\cdot\boldsymbol{\mu}_{\shortparallel}|^2 \rho(\varphi) \, d\zeta d\gamma d\varphi \\
&\propto 8\sin^2\theta\cos^2\theta - (3\sin^4\theta - 24\sin^2\theta\cos^2\theta + 8\cos^4\theta) \left\langle \sin^4\varphi \right\rangle \\
&\quad + 4(\sin^4\theta - 7\sin^2\theta\cos^2\theta + 2\cos^4\theta) \left\langle \sin^2\varphi \right\rangle
\end{aligned}
\tag{2.18}
$$

$$
\begin{aligned}
I_{VV}^{\perp\perp} &\propto \int_0^{\frac{\pi}{2}} \int_0^{2\pi} \int_0^{2\pi} I_{ex} |\boldsymbol{E}\cdot\boldsymbol{\mu}_{\perp}|^2 \, I_{em} |\boldsymbol{E}\cdot\boldsymbol{\mu}_{\perp}|^2 \rho(\varphi) \, d\zeta d\gamma d\varphi \\
&\propto \int_0^{\frac{\pi}{2}} \int_0^{2\pi} \int_0^{2\pi} |\boldsymbol{E}\cdot\boldsymbol{\mu}_{\perp}|^4 \rho(\varphi) \, d\zeta d\gamma d\varphi \\
&\propto (8 - 28\sin^2\theta + 23\sin^4\theta) \left\langle \sin^4\varphi \right\rangle \\
&\quad + (32\sin^2 - 40\sin^4\theta) \left\langle \sin^2\varphi \right\rangle + 8\sin^4\theta
\end{aligned}
\tag{2.19}
$$

In VH configuration, similarly we can obtain the polarization dependence of four cases $I_{VH}^{\parallel\parallel}$, $I_{VH}^{\parallel\perp}$, $I_{VH}^{\perp\parallel}$ and $I_{VH}^{\perp\perp}$ as

$$
\begin{aligned}
I_{VH}^{\parallel\parallel} &\propto \int_0^{\frac{\pi}{2}} \int_0^{2\pi} I_{ex} |\boldsymbol{E}\cdot\boldsymbol{\mu}_{\shortparallel}|^2 \, I_{em} |\boldsymbol{f}\cdot\boldsymbol{\mu}_{\shortparallel}|^2 \rho(\varphi) \, d\gamma d\varphi \\
&\propto \int_0^{\frac{\pi}{2}} \int_0^{2\pi} |\boldsymbol{E}\cdot\boldsymbol{\mu}_{\shortparallel}|^2 \, |\boldsymbol{f}\cdot\boldsymbol{\mu}_{\shortparallel}|^2 \rho(\varphi) \, d\gamma d\varphi \\
&\propto \frac{3}{4}\sin^2\theta\cos^2\theta \left\langle \sin^4\varphi \right\rangle + 2\cos^2\theta\sin^2\theta \left\langle \cos^4\varphi \right\rangle \\
&\quad + (\sin^4\theta + \cos^4\theta - 4\sin^2\theta\cos^2\theta) \left\langle \sin^2\varphi\cos^2\varphi \right\rangle
\end{aligned}
\tag{2.20}
$$

$$
\begin{aligned}
I_{VH}^{\parallel\perp} &\propto \int_0^{\frac{\pi}{2}} \int_0^{2\pi} \int_0^{2\pi} I_{ex} |\boldsymbol{E}\cdot\boldsymbol{\mu}_{\shortparallel}|^2 \, I_{em} |\boldsymbol{f}\cdot\boldsymbol{\mu}_{\perp}|^2 \rho(\varphi) \, d\zeta d\gamma d\varphi \\
&\propto 4(7\sin^2\theta\cos^2\theta - 3\cos^4\theta) \left\langle \sin^2\varphi \right\rangle \\
&\quad + (4\sin^4\theta - 27\sin^2\theta\cos^2\theta + 4\cos^4\theta) \left\langle \sin^4\varphi \right\rangle + 8\cos^4\theta
\end{aligned}
\tag{2.21}
$$

$$
\begin{aligned}
I_{VH}^{\perp\parallel} &\propto \int_0^{\frac{\pi}{2}} \int_0^{2\pi} \int_0^{2\pi} I_{ex} |\boldsymbol{E} \cdot \boldsymbol{\mu}_{\perp}|^2 \, I_{em} |\boldsymbol{f} \cdot \boldsymbol{\mu}_{\parallel}|^2 \rho(\varphi) \, d\zeta d\gamma d\varphi \\
&\propto 4(7\sin^2\theta\cos^2\theta - 3\sin^4\theta) \left\langle \sin^2\varphi \right\rangle \\
&\quad + (4\sin^4\theta - 27\sin^2\theta\cos^2\theta + 4\cos^4\theta) \left\langle \sin^4\varphi \right\rangle + 8\sin^4\theta
\end{aligned}
\tag{2.22}
$$

$$
\begin{aligned}
I_{VH}^{\perp\perp} &\propto \int_0^{\frac{\pi}{2}} \int_0^{2\pi} \int_0^{2\pi} I_{ex} |\boldsymbol{E} \cdot \boldsymbol{\mu}_{\perp}|^2 \, I_{em} |\boldsymbol{f} \cdot \boldsymbol{\mu}_{\perp}|^2 \rho(\varphi) \, d\zeta d\gamma d\varphi \\
&\propto 4 - 6\sin^2\theta\cos^2\theta + 3(27\sin^2\theta\cos^2\theta - 4) \left\langle \cos^4\varphi \right\rangle \\
&\quad + 2(4 - 21\sin^2\theta\cos^2\theta) \left\langle \cos^2\varphi \right\rangle
\end{aligned}
\tag{2.23}
$$

The results by using dipole approximation can be applied to polarization study of Raman spectroscopy from the sample with any distribution. According to the selection rules for first-order Raman scattering, the following phonon modes can be observed in both VV and VH configurations, A mode in agreement with "$\parallel\parallel$" case, A and E_2 modes in agreement with "$\perp\perp$" case, and E_1 mode in agreement with "$\parallel\perp$" and "$\perp\parallel$" cases.

Chapter 3

Polarized Raman spectroscopy of vertically aligned single-walled carbon nanotubes

3.1 Background of this research

It is reported by Murakami *et al.* [18, 20] that the 180 cm^{-1} peak in Raman spectroscopy under 488 nm laser excitaion is characteristically observed for in VA-SWNTs sample, which was explained by the resonance of $\Delta\mu = \pm 1$ excitation (μ denotes the cutting line index of the 2D Brillouin Zone of graphite). Since it is very sensitive to the morphology of sample, vertical alignment could be simply recognized by Raman spectroscopy without resorting to SEM observation which would be a quick and non-destructive means. However, at that time the sample was not long enough (about 5 μm) for careful experiment, and also the polarized Raman measurements did not discuss about the polarization dependence of peak intensity quantitively. Furthermore, the lack of calculation and experimental data of Kataura plot makes the perpendicularly-polarized excitation assumption uncertain in some extent.

Recently, this 180 cm^{-1} peak is found to be composed of at least four sharp peaks under high resolution Raman measurement (see Fig. 3.1). When the alignment is ruined such as dispersed in D_2O solution and dried, the 180 cm^{-1} peak disappears. Also, if the sample is placed in air for long time like two years, the Raman spectrum does not show the

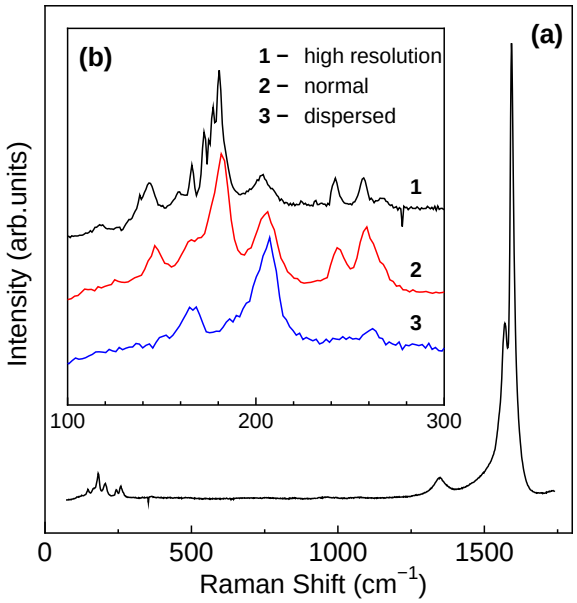

Figure 3.1: Raman spectroscopy taken from top of VA-SWNTs shown as (a); the inset figure shows RBM range under high resolution(plot 1), and under normal resolution before (plot 2) and after dispersed(plot 3).

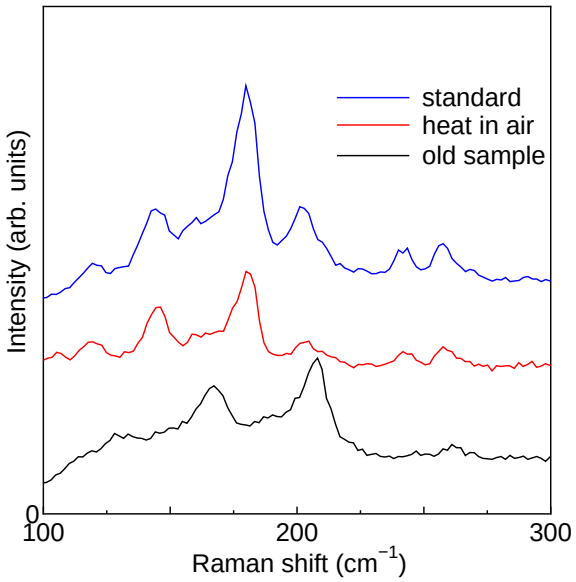

Figure 3.2: RBM range of Raman spectroscopy taken from top of VA-SWNTs from the sample placed in air for two years and after annealed at 300°.

180 cm^{-1} peak. But after heating it at 300 ° C in air for 10 minutes and then taking Raman spectrum, it recovers (Fig. 3.2). It can be explained by the molecule adsorption to the CNT

surfaces, which changes the electronic structure so that it is no longer resonant with the 488 nm laser [20].

In this experiment, we try to reveal the origin of this abnormal peak and explore the polarization dependence in Raman spectra by carrying out specific polarized configuration and quantitive analysis.

3.2 Experiment Settings

3.2.1 Raman spectrometer

Micro Raman spectrometer is used in the experiment which is composed by three parts: laser source, optical microscope Raman system, and the scattering detecting system as shown in Fig. 3.3. The laser is introduced passing several optics and focused to the sample surface. The back scattered lights are collected through the same lenses as incident light, then sent to the monochromater and recorded by a CCD. In the incident light path, a bandpass filter is inserted to cut off laser lines other than the main-wavelength light in the laser source. Before entering the monochromater, the intense Rayleigh signal is filtered by a dichroich mirror and an adjustable notch filter.

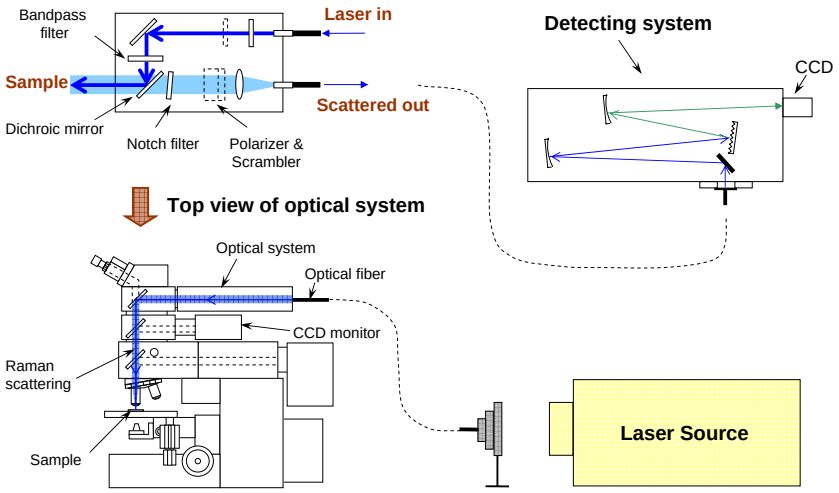

Figure 3.3: Scheme of Raman spectrometer

3.2.2 Experiment Sample

The sample investigated in this experiment is vertically aligned single-walled carbon nanotubes prepared by ACCVD method which has thickness about 13 μm (Fig. 3.4).

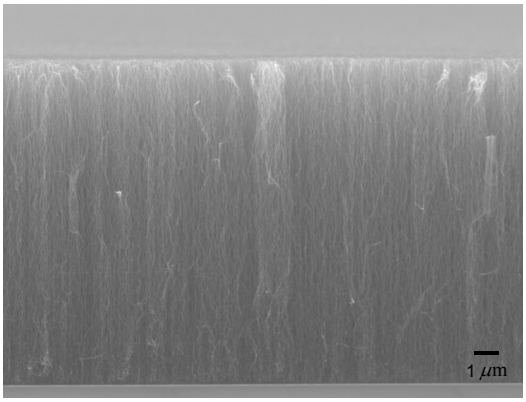

Figure 3.4: SEM image of VA-SWNTs

3.2.3 Polarized Raman measurement configurations

The sample substrate is positioned standing on the rotation stage so that the laser is injected on the side of VA-SWNT film (Fig. 3.5).

Incident light polarization is maintained through optical fiber and a polarizer with scrambler is inserted to select the observation orientation. When incident light and polarizer orientation for observing scattered light are parallel, we call it VV configuration; when they are perpendicular to each other, we call it VH configuration. The angle between incident light polarization and SWNT growth direction is called θ. By rotating the stage, we can change θ from 0° to 90° and observe the polarization dependence of each vibration mode peak in Raman spectra in VV and VH configurations. A 488nm Argon laser is used as incident light source with the power of 0.2 mW at the sample surface under $50\times$ objective lens where the laser spot is about 2 μm in diameter .

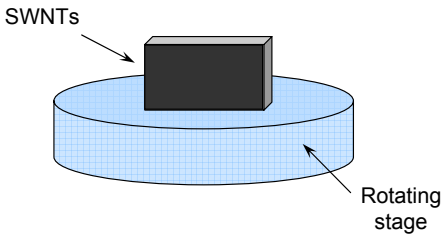

(a) Scheme of SWNTs on rotating stage

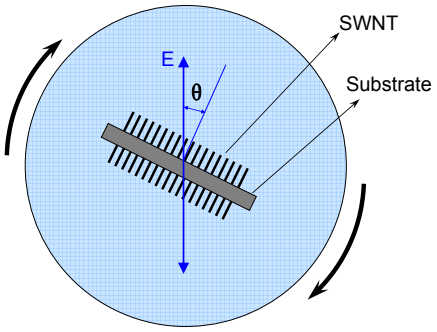

(b) Top view of rotating stage with VV configuration

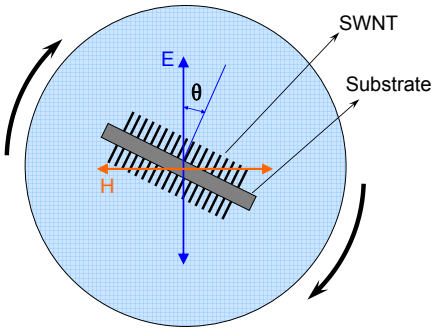

(c) Top view of rotating stage with VH configuration

Figure 3.5: Scheme of polarized raman measurement configurations

3.3 Results and Analysis

3.3.1 Raman spectra from VV and VH configurations

By rotating the sample from 0° to 90° by 15° a series of Raman spectra are obtained in both VV (Fig. 3.6) and VH configuration (Fig. 3.7). Considering that the laser spot might displace during the rotation caused by mechanical error, three times measurements were taken at each angle and an average value was gained to plot the spectra.

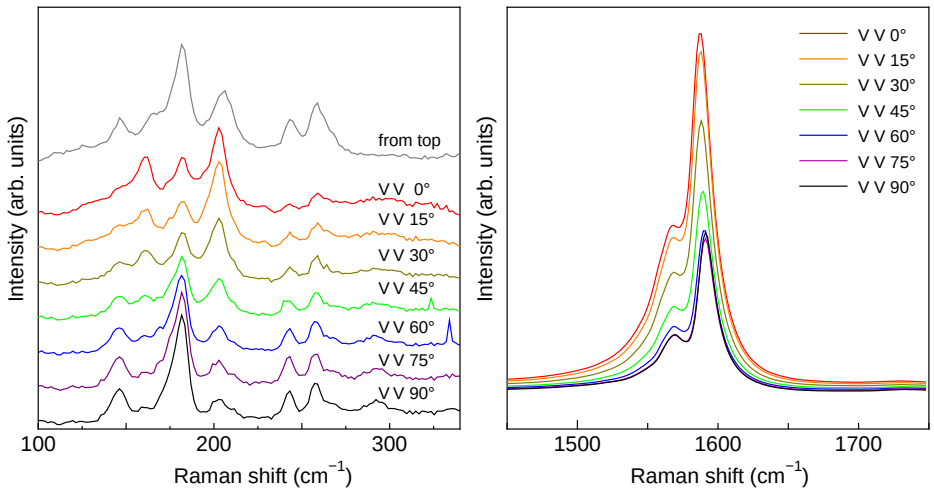

(a) RBM (b) G-band

Figure 3.6: Raman spectra of a VA-SWNT film in the VV configuration, and changing the incident polarization from 0° (along alignment direction) to 90° (perpendicular to the alignment direction)

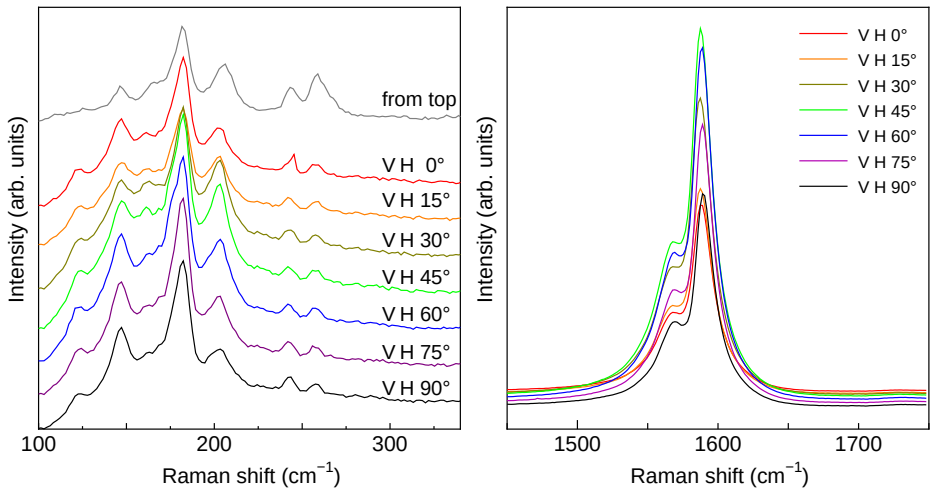

(a) RBM (b) G-band

Figure 3.7: Raman spectra of a VA-SWNT film in the VH configuration, and changing the incident polarization from 0° (along alignment direction) to 90° (perpendicular to the alignment direction)

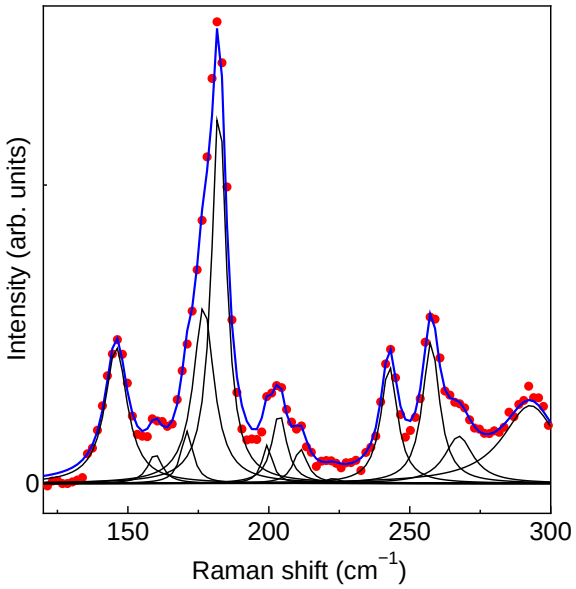

Figure 3.8: Decompositon of RBM peaks into Lorentzian curves in which peak positions are determined from high resolution Raman spectrum(Fig. 3.1)

3.3.2 RBM

In VV configuration, it can be clearly seen from RBM range that two groups of peaks behave oppositely in changing from 0 ° to 90 °: the intensity of {160, 203 cm^{-1}} peaks(noted as {203 cm^{-1}} group) decrease while intensity of {145, 181, 244, 256 cm^{-1}} peaks(noted as {181 cm^{-1}} group) increase. If all the SWNTs are well aligned in the growth direction and obey the parallel excitation as well accepted, we should see all the RBM peaks behave the same trend during the rotation as {203 cm^{-1}} group. The anomaly attracts our attention and leads to two assumptions. One attributes it to the perpendicularly-polarized excitation [20, 16], which means SWNT absorbs light polarized to the tube axis, thus it would absorb the most when polarization angle is 90° and least at 0°. Moreover according to the selection rule, the RBM (A mode) is allowed to be observed in ($\boldsymbol{XX}$) configuration, in which both incident and scattered light are perpendicular to the tube axis. By carefully decomposing RBM peaks into Lorentzian curves (Fig. 3.8), intensity dependence on polarization angle can be plotted in which each peak's intensity is normalized by the strongest peak (Fig. 3.9). In previous chapter, we obtain the formulae for describing the relationship between scattered light intensity and polarization angle corresponding to different transition types in VV and VH configurations. Here, we apply the $I_{VV}^{\parallel\parallel}$ relation

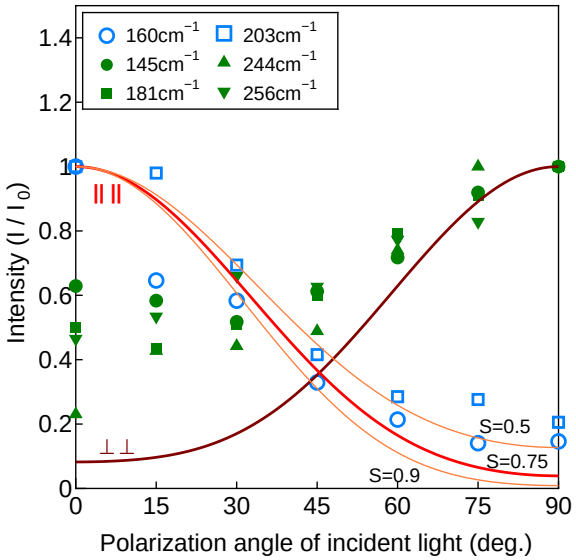

Figure 3.9: RBM Peak intensity changes for incident light polarization from 0° to 90° with respect to the VA-SWNT growth direction (VV configuration)

(Eqn.2.16)

$$I_{VV}^{\parallel\parallel} \propto 2\cos^4\theta \left\langle \cos^4\varphi \right\rangle + 6\cos^2\theta \sin^2\theta \left\langle \sin^2\varphi \cos^2\varphi \right\rangle + \frac{3}{4}\sin^4\theta \left\langle \sin^4\varphi \right\rangle$$

and the $I_{VV}^{\perp\perp}$ relation (Eq. 2.19)

$$I_{VV}^{\perp\perp} \propto (8 - 28\sin^2\theta + 23\sin^4\theta) \left\langle \sin^4\varphi \right\rangle + (32\sin^2 - 40\sin^4\theta) \left\langle \sin^2\varphi \right\rangle + 8\sin^4\theta$$

to the plot by considering a Guassian distribution function and utilize a so called "nematic order parameter" $S = \frac{1}{2}(3\left\langle \cos^2\varphi \right\rangle - 1)$ to indicate the alignment of the VA-SWNT film. The order parameter $S = 0.75$ in the VA-SWNTs has been proved by optical absorption[21] and X-ray absorption[22]. From Fig. 3.9, it can be seen that $\{203\,\mathrm{cm}^{-1}\}$ group peaks behave close to the assumption of parallel excitation. However, the $\{181\,\mathrm{cm}^{-1}\}$ group peaks deviate much from cross-polarized excitation assumption even though taking into account the possible errors in background subtraction and peak decomposition.

Similarly, RBM peaks in VH configuration can be decomposed and plotted as a function of polarization angle (Fig. 3.10). Both parallel and cross-polarized excitation give maximum at 45° which is the trends all the plots exhibit. Similarly as shown in VV configuration, the $\{181\,\mathrm{cm}^{-1}\}$ group peaks behave much deviate from the cross-polarized assumption curve with order parameter $S = 0.75$.

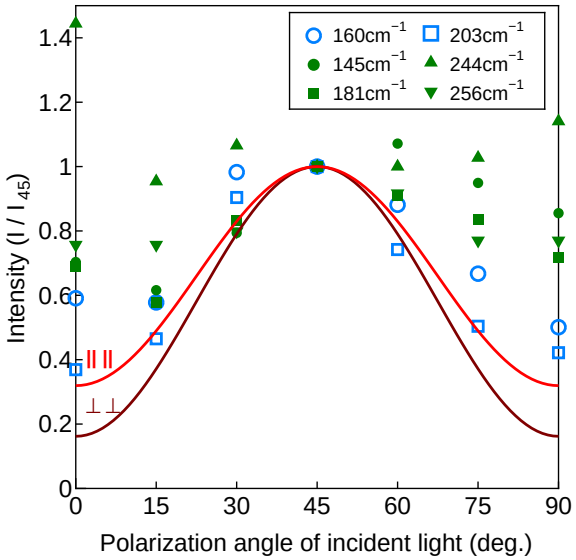

Figure 3.10: RBM Peak intensity changes for incident light polarization from 0° to 90° with respect to the VA-SWNT growth direction (VH configuration)

Kataura plot also helps to assign most of the chiralities. Here, we adapt $\omega_{RBM} = \frac{217.8}{d_t} + 15.7$ to the Kataura plot which can appropriately describe the relationship between tube diameter and the Raman shift of RBM peaks of VA-SWNTs sample [10]. From the plot, it can be seen that several CNTs around 180 cm^{-1} are resonant with 2.5 4eV, which could be responsible to assign those sharp peaks observed in RRS under high resolution. And {203 cm^{-1}} group peaks can also be found in resonance window. So far the lack of empirical and calculation data about $\mu \pm 1$ transition makes it difficult to discuss the assignment with corss-polorized excitation. But the capacity to assign the most abnormal strongest peak of 180 cm^{-1} in normal Kataura plot provides brand new information compared with Murakami *et al.*'s report.

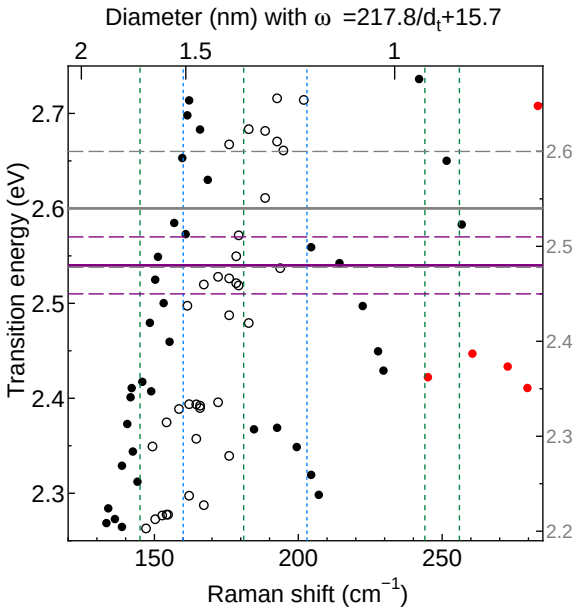

Figure 3.11: Kataura plot of E_{ii} transition using the equation $\omega_{RBM} = \frac{217.8}{d_t} + 15.7$ to describe the relation of tube diameter and Raman shift. Red filled , black open, and black filled circles stand for metallic[$(2n+m)$mod3 $= 0$], semiconducting type-I[$(2n+m)$mod3 $= 1$], and semiconducting type-II SWNTs[$(2n+m)$mod3 $= 2$] respectively. The violet solid line denotes the excitation energy 2.54eV of 488nm laser, and the violet dash lines denote the resonance window. Bundling causes resonant energy to redshift by 60meV and resonance window broaden by 120meV which is denoted by grey solid line and dash lines[23].

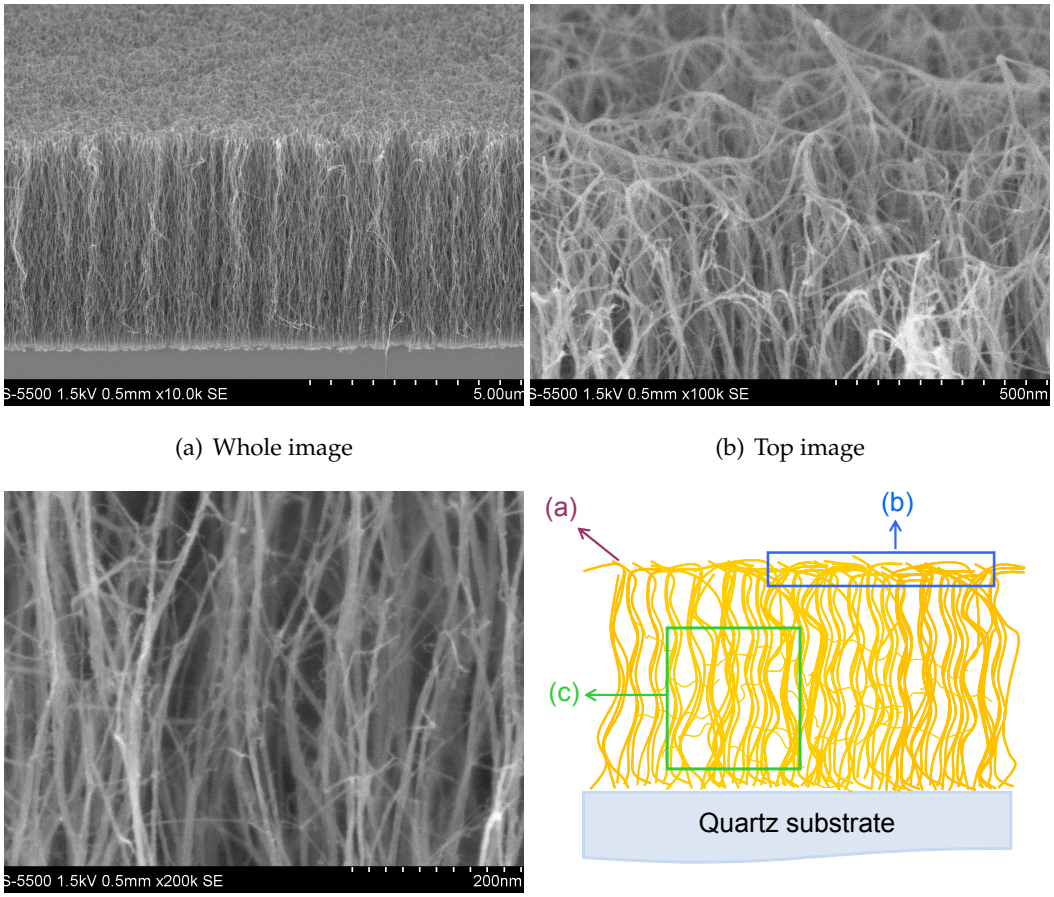

(a) Whole image

(b) Top image

(c) Middle image

(d) Schematics of VA-SWNTs morphology

Figure 3.12: SEM image of (a) whole, (b) top part, and (c) middle part of VA-SWNTs under high resolution and a scheme of morphology of VA-SWNTs based on SEM images

Further more, the high resolution SEM images reveal that some SWNTs are suspending among the forest of well aligned SWNTs, which might be isolated or small bundled (Fig. 3.12). Those SWNTs could be responsible to the abnormal behavior in RBM in VV configuration, and their imperfect alignment might cause the deviation from theoretical calculation.

3.3.3 G-band

Another important feature of SWNT Raman spectroscopy is tangential G-band (Fig. 3.6(b), 3.7(b)), which is composed of several phonon modes of symmetries $A(A_g)$ $E_1(E_{1g})$ and $E_2(E_{2g})$ for chiral (achiral) SWNTs. According to the group theory and selection rules, A mode can be observed in ($\boldsymbol{ZZ}$) symmetry, E_2 mode can be observed in ($\boldsymbol{XX}$) symmetry, and E_1 mode can be observed in ($\boldsymbol{XY}$) or ($\boldsymbol{YX}$) symmetry. Therefore the polarization dependence for each mode is expected to be observed by adjusting the geometry settings. In bundled SWNTs, A and E_1 mode can not be clearly separated because their frequencies are overlapped [15]. Here we decompose G-band into six peaks as shown in Fig. 3.13: four Lorentzians for semiconducting SWNTs noted as G^+ ($A + E_1$) at 1590 cm^{-1}, G^- ($A + E_1$) at 1567 cm^{-1}, E_2^+ (E_2) at 1607 cm^{-1}, and E_2^- (E_2) at 1549 cm^{-1}; and a Lorentzian noted as $G^+_{metallic}$ (A) at 1591 cm^{-1}, and an asymmetric Breit-Winger-Fano(BWF) at 1561 cm^{-1} for metallic SWNTs [11].

The typical G-band peak intensities are plotted as the function of polarization angle in Fig. 3.14. It is found that G^+, G^-, and $G^+_{metallic}$ peaks all behave as A mode indicated as the brown curve, i.e. light absorption and emission all parallel to the SWNT axis. The E_2 mode can be distinguished only when incident and scattered light are both perpendicular

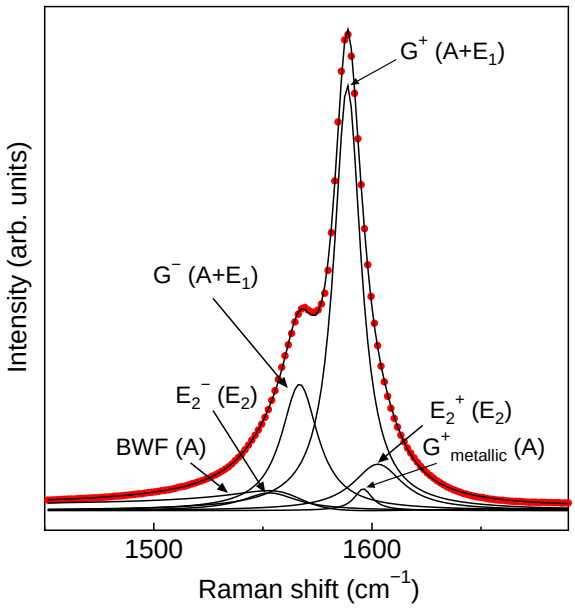

Figure 3.13: Decomposition of G-band

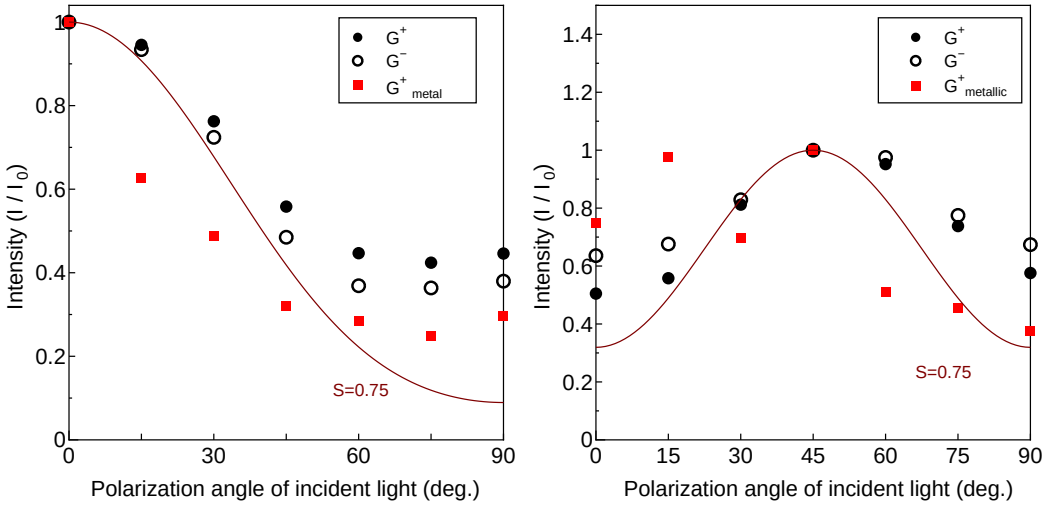

(a) VV configuration

(b) VH configuration

Figure 3.14: G-band peak intensity as the function of incident light polarization angle in (a)VV and (b)VH configurations

to the tube axis and in resonance with $E_{\mu\mu\pm1}$ optical transition. However, the intensity are strongly reduced due to the depolarization effect in that case [24]. Thus, A mode is the dominant mode in G-band features. It is found a deviation by about 40% from theoretical calculation with a order parameter 0.75 in Fig. 3.14, which can be attributed to several possible reasons such as suspended SWNTs within the VA-SWNT forest, the mixed of E_1 mode behaviar, and temperature effect by laser heating (see discussion in Chapter 4).

Chapter 4

Temperature effect on polarized Raman spectroscopy

4.1 Temperature dependence in SWNT Raman spectroscopy

When measuring Raman spectroscopy, the SWMT sample is easy to be heated by the laser irradiation. And it is found that at high temperature, the anharmonic components of bonding force become prominent, which induce the thermal expansion and thus decrease the Raman shift frequency [7]. The decomposed six G-band peaks from HiPco sample all behave decreasing as temperature increases. And all the G^+ peak measured from different SWNT sample show the same dependence with temperature [25], which can be fitted with the function

$$\omega(T) = \omega_0 - \frac{A}{exp(B\hbar\omega_0/k_BT) - 1} \tag{4.1}$$

where $\hbar$ is Planck's constant, k_B is Boltzmann constant, T is the sample temperature, $\omega_0 = 1594\,cm^{-1}$, $A = 38.4\,cm^{-1}$, and $B = 0.438$. Therefore, it is easy to know the sample temperature by inspecting the G^+ Raman shift. Moreover, the difference in Raman shift between G^+ and G^- peaks is usually used to identify the diameter change in semiconducting SWNT sample, which has the relation expressed as

$$\omega_{G^+} - \omega_{G^-} = \frac{\alpha}{d_t^2} \tag{4.2}$$

where d_t is the nanotube diameter, α is a proportional coefficient. The $\omega_{G^+} - \omega_{G^-}$ are observed slightly increasing with temperature in 488 nm and 514 nm excitation in HiPco

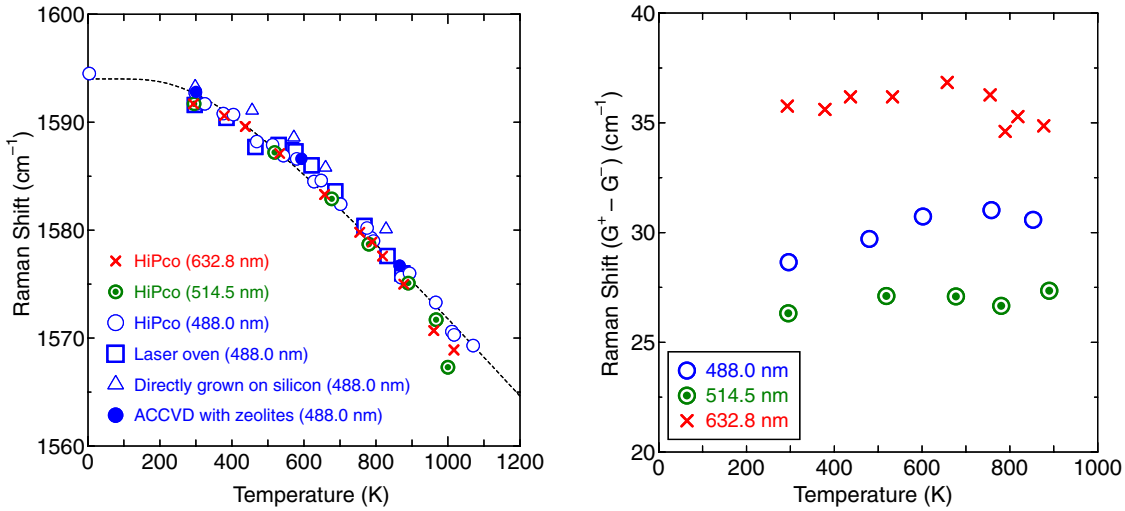

Figure 4.1: (a) Temperature dependence of Raman shifts of G^+ peaks for various SWNT samples measured with a 488.0 nm excitation laser and for HiPco sample measured with three excitation lasers (488.0, 514.5, and 632.8 nm). The dashed line is a fitting line calculated using equation 4.1. (b) Temperature dependence of differences between G^+ and G^- peaks, measured with three excitation lasers. [25]

sample (Fig. 4.1(b)), which means more small diameter semiconducting SWNTs are in resonance at high temperature. The temperature change also affects the Raman intensity, which can be described as

$$I = I_0\, exp(-\frac{T}{B}) = I_0\, exp(-\frac{T}{430}) \tag{4.3}$$

where T is the sample temperature, I_0 denotes the Raman intensity in 0 K, and the constant B is fitted with 430 in this case.

4.2 Temperature effect on G-band in polarized Raman spectroscopy

Inspecting each peak frequency of the six G-band peaks, we found that most of the peaks appear increasing in Raman shift when incident polarization angle changes from 0 °to 90 °, especially G^+ peak changes from 1587.6 to 1591.5 cm^{-1} in VV configuration (Fig. 4.2(a)). It is because SWNTs absorb more light polarized along the tube axis, and thus causes the heating to the sample. Applying the equation 4.1, the sample temperature can be estimated changing from about 500 K at 0 ° to 360 K at 90 ° (as indicated in the

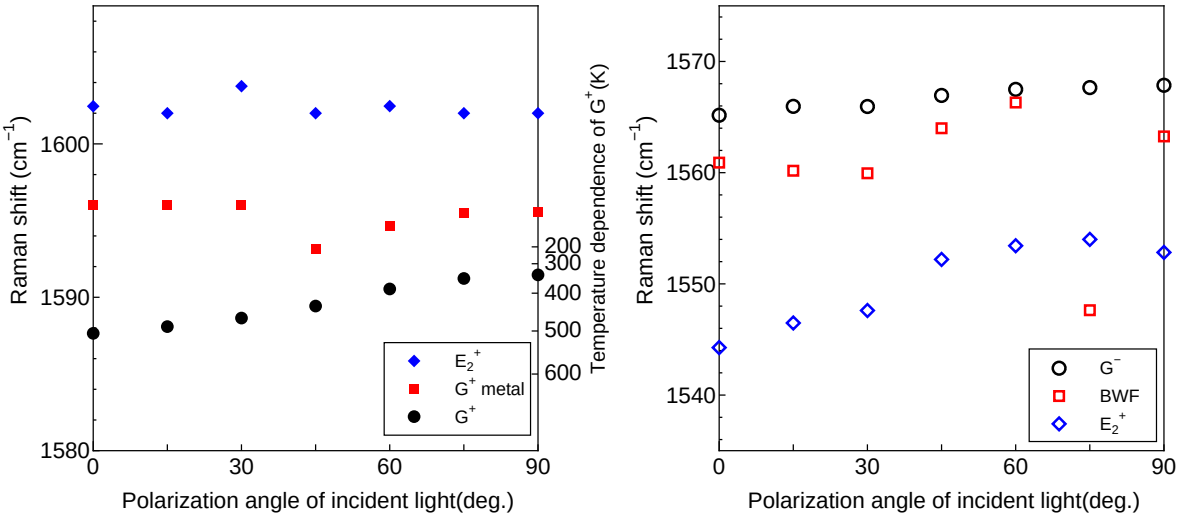

(a) VV

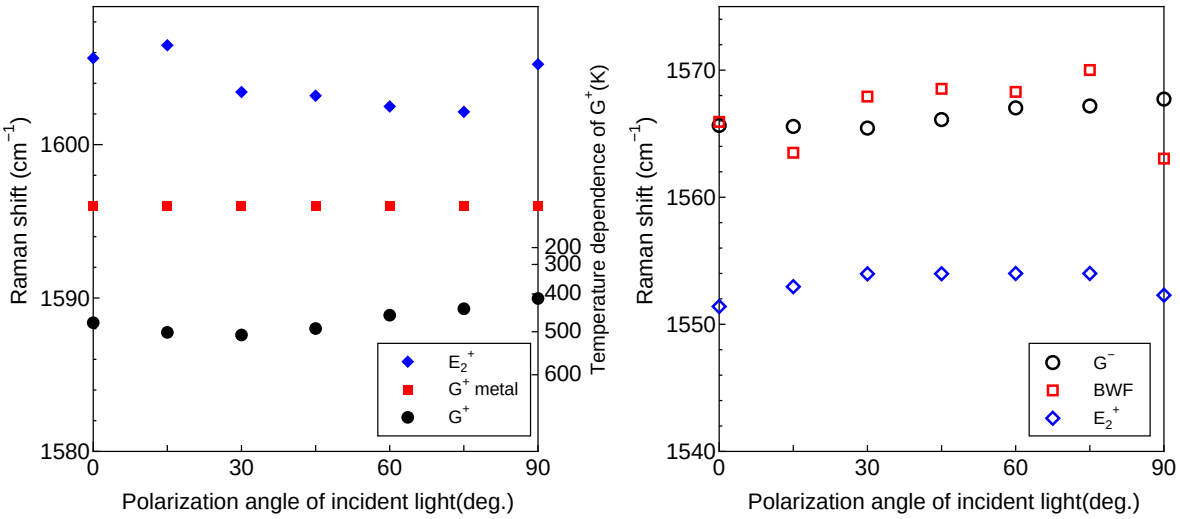

(b) VH

Figure 4.2: Raman shift changes of six G-band peaks with respect to the incident polarization angle in (a) VV and (b) VH configurations. The Right coordination indicates the sample temperature calculated by Eqn. 4.1.

right coordination in Fig. 4.2). In VH configuration, G^+ peak frequency shows the similar increasing trends from 1587.6 to 1590 cm^{-1}(Fig. 4.2(b)).

Applying the temperature effect to the Raman intensity, a corrected G^+ peak intensity as the function of incident polarization angle is plotted in Fig. 4.3. After correction,

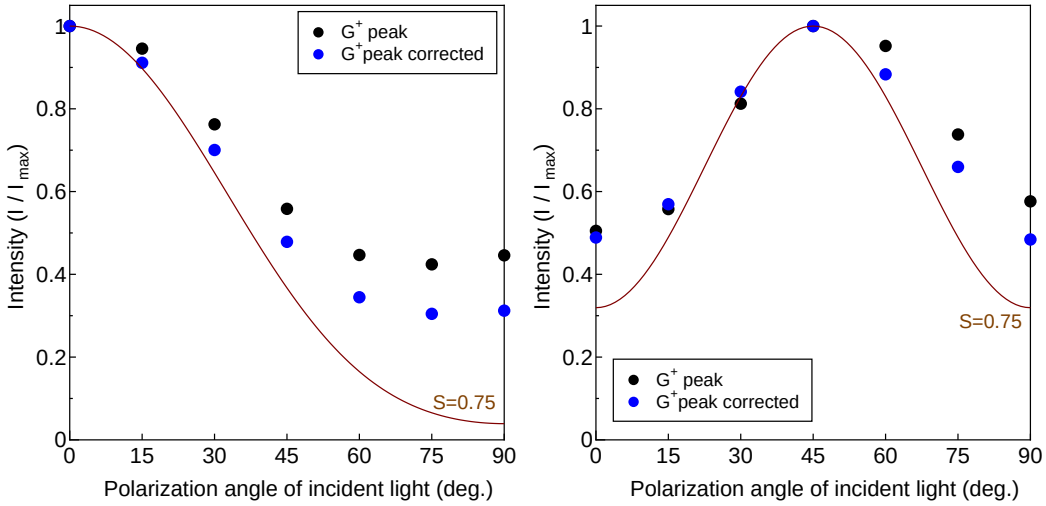

(a) VV (b) VH

Figure 4.3: G^+ peak intensity before (black dot) and after correction (blue dot) with temperature effect (Eqn. 4.3) in (a) VV and (b) VH configurations.

G^+ peak intensities appear closer to the theoretical calculation result both in VV and VH configurations.

The difference in Raman shift between G^+ and G^- peaks is also obtained as shown in Fig. 4.4. It shows 1.5 cm^-1 shift up from 0 °to 90 °in VV configuration.

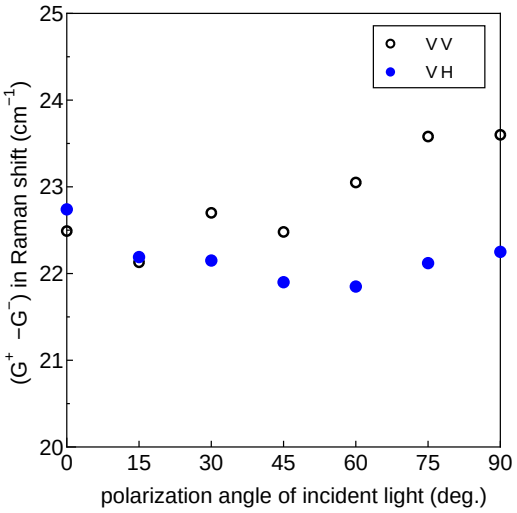

Figure 4.4: Differences between G^+ and G^- peak frequency with respect to incident polarization angle in VV and VH configurations.

4.2.1 Temperature effect on RBM in polarized Raman spectroscopy

It is reported that RBM peaks have two types behaviors in HiPco sample: intensity increasing or decreasing when temperature increases [7]. Here, the temperature dependence of VA-SWNTs sample was measured by using laser heating. From the Raman spectra, the sample temperature can be calculated from G^+ peak frequency (Eqn. 4.1), and therefore a temperature effect-corrected G^+ peak intensity can be obtained (Eqn: 4.3). Since increasing laser power not only increases the sample temperature, but also increases the Raman intensity, to obtain the real intensity dependence on temperature, it is necessary to remove the effect of laser power. Noting that G^+ and RBM peaks are enhanced by the same times by laser power, this effect can be removed by normalized with temperature-corrected G^+ peak intensity. In Fig. 4.5, it shows the temperature dependence of five main RBM peaks in VA-SWNTs sample with 488 nm excitation. 203 cm^{-1} peak behaves constant before 800 K, while {145, 180, 245, 256 cm^{-1}} group peaks decrease almost linearly by about 80% before 720 K and become constant at higher temperatures.

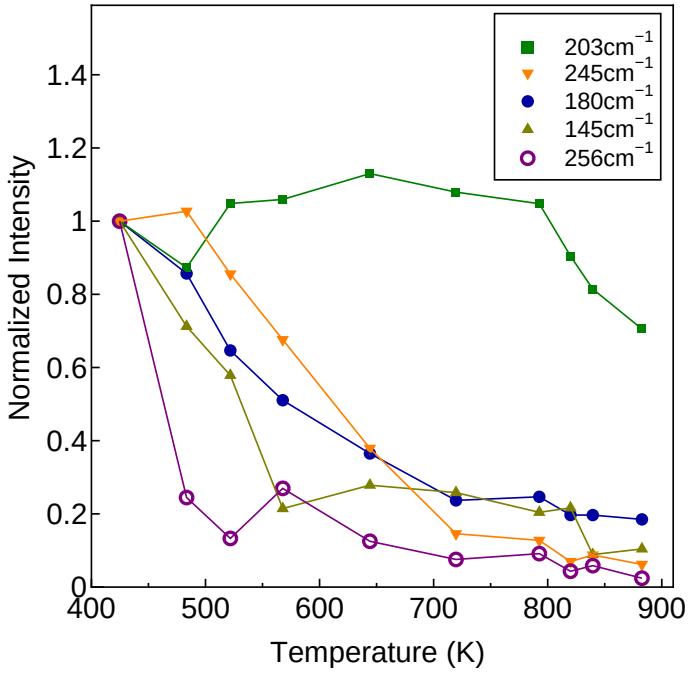

Figure 4.5: RBM peak intensity dependences on temperature in VA-SWNTs sample, normalized by the peak intensity at 424 K.

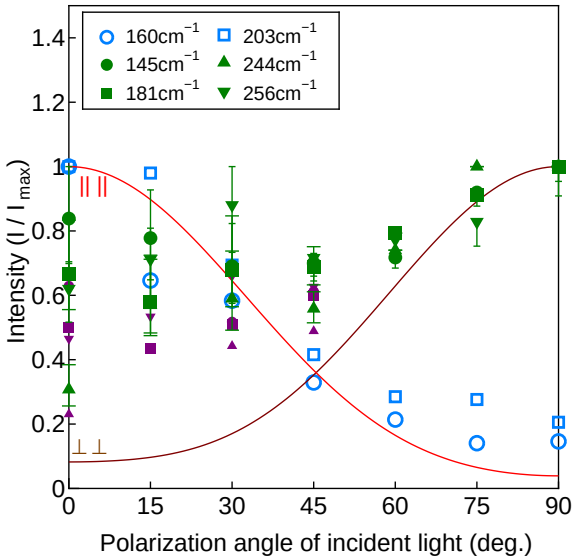

Figure 4.6: Corrected RBM intensities (in green) for temperature effects, compared with the data before correction (in purple) in VV configuration.

Then we try to apply this temperature effect to the RBM intensities in VV spectra. Noticing that light absorption gives rise to the different temperature at each polarization angle, data points from 0° (509 K) to 60° (403 K) of {180 cm^{-1}} group was corrected by considering a linear decreasing of 0.35/100 K from 400 K to 500 K (based on Fig. 4.5). The corrected results in Fig. 4.6 shows that the real RBM intensities of {180 cm^{-1}} group peaks tend to be constant and independent of polarization angle, which indicates the suspended SWNTs in the VA-SWNT forest are randomly distributed. This morphology has been seen in FE-SEM images (Fig. 3.12).

Chapter 5

Polarized Raman spectroscopy of CoMoCat SWNTs in stretched PVA film

5.1 Motivation of this work

In order to extensively investigate on the polarization dependence of RBM peak, the aligned SWNTs sample was made by stretching SWNT-suspended PVA (polyvinyl alcohol) film [26, 27, 28]. Then polarized optical absorption and polarized Raman measurements were carried out with this sample.

5.2 Experiment

The CoMoCat-grown SWNTs 20 mg were dispersed in 10 mg D_2O with 1wt% SDBS (Sodium dodecylbenzene sulphonate) by sonicating with an ultrasonic processor (Hielscher GmbH, UP-400S with H3/Micro Tip 3) for 30 minutes at a power flux level of 368 W/cm^2 (80% amlification). Then the dispersion was ultra centrifuged (Hitachi Koki himac CS120GX with a S100ST6 angle rotor) for 1 hour under 60,000 rpm and the supernatants were collected. PVA powder (Wako Pure Chemical Industry, polymerization degree 1500) in 15wt% was disolved in distilled water at 80 °C water bath for 10 minutes and cooled down to the room temperature. Then it was added into SWNT-suspension and well

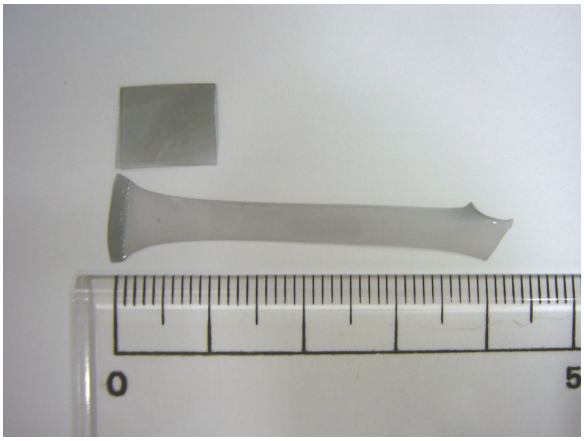

Figure 5.1: The CoMoCat-PVA film before and after stretching

mixed using a pipette. The resulting solution was poured into a Petri dish and evaporated at room temperature for 24 hours. The formed black-color film was removed and gradually stretched on a heated cylindral metal surface at about 80°C. The stretching ratio was about 4 to 5 (see Fig. 5.1).

5.3 Optical Absorption

The Fig. 5.2 shows the optical absorption spectra from the CoMoCat-PVA film by using incident light polarized parallel and perpendicular to the stretching direction. The extremely weak absorbance by perpendicularly-polarized light indicates that most of the SWNTs are aligning in the stretching direction and behaving as the "antenna". Recalling the equation 2.14,

$$\frac{I_{exp}(0) - I_{exp}(\frac{\pi}{2})}{I_{exp}(0) + 2_{exp}I(\frac{\pi}{2})} = \frac{\Lambda_{\shortparallel} - \Lambda_{\perp}}{\Lambda_{\shortparallel} + 2\Lambda_{\perp}}(\frac{3\left\langle \cos^2\varphi - 1\right\rangle}{2}) = \frac{\Lambda_{\shortparallel} - \Lambda_{\perp}}{\Lambda_{\shortparallel} + 2\Lambda_{\perp}} \cdot S, \tag{5.1}$$

we can estimate the order parameter from the optical absorption spectra. Adopting that $\Lambda_{\parallel}/\Lambda_{\perp} \approx 10$ in the E_{11} energy region [21], we choose the largest absorption at around 1.2 eV (E_{11} of (6,5) nanotube) in the spectra to calculate the order parameter. Since $I_{exp}(\frac{\pi}{2})$ is very small, it gives rise to a order parameter $S \approx 1$, which indicates a preeminent alignment can be achieved by stretching technique.

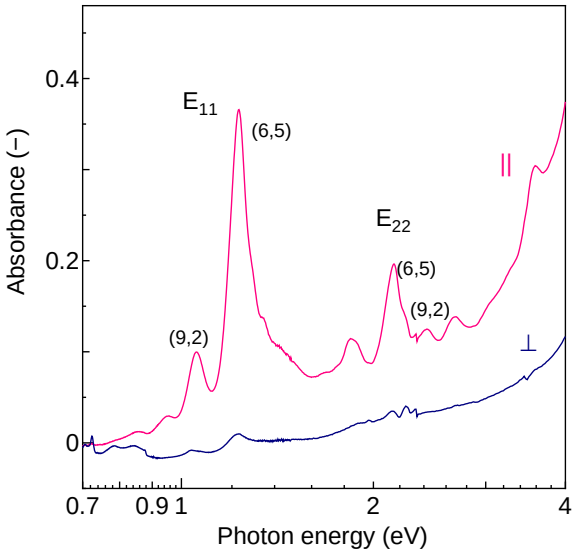

Figure 5.2: Optical absorption spectra from the stretched CoMoCat-PVA film with incident light polarized parallel (∥) and perpendicular (⊥) to the stretching direction.

5.4 Polarized Raman spectroscopy

Since the alignment of SWNTs was achieved by stretching technique which was proved by optical absorption, it provides a comparable sample to check polarization dependence of Raman measurement additively. The same experiment settings as VA-SWNTs of VV and VH configurations were applied on the CoMoCat-PVA film by using 488 nm Laser. The result spectra is shown as Fig. 5.3 and Fig. 5.4.

In RBM range, the low optical density causes relatively high noise/signal ratio though, it is clear to see a strong 305 cm^{-1} peak (from (7,4) nanotube [29]) and small peaks around 248 cm^{-1}(from (7,7) nanotube) and 265 cm^{-1} (from (8,5) nanotube) all appearing as parallel excitation in which peak intensity decreases as the polarization angle changes from 0 °to 90 °. In VH configurations the strong 305 cm^{-1} peak can be distinguished rather than others and shows the maximum intensity at 45 °.

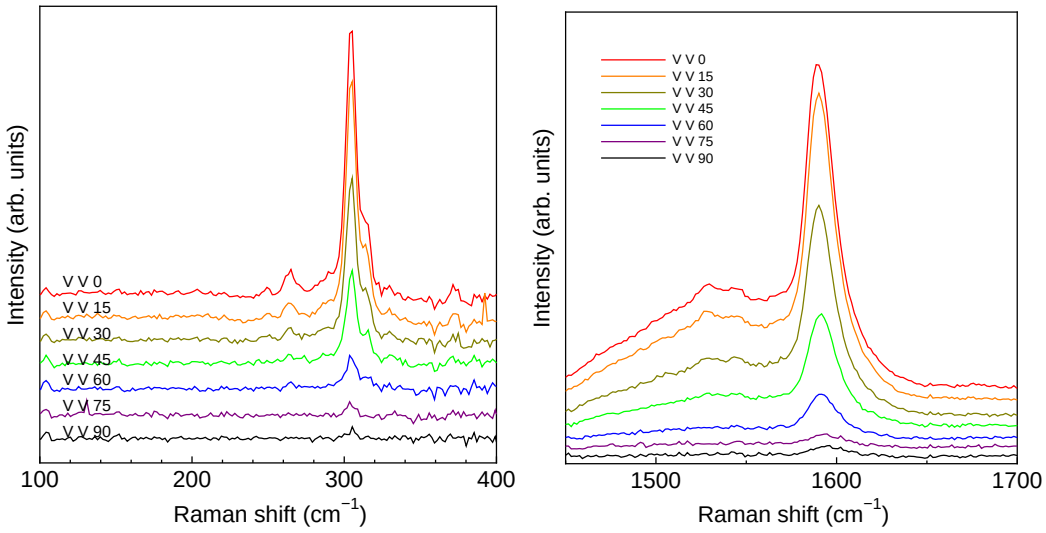

(a) RBM (b) G-band

Figure 5.3: Raman spectra of the stretched CoMoCat-PVA film in the VV configuration with the incident polarization changing from 0° (along alignment direction) to 90° (perpendicular to the alignment direction).

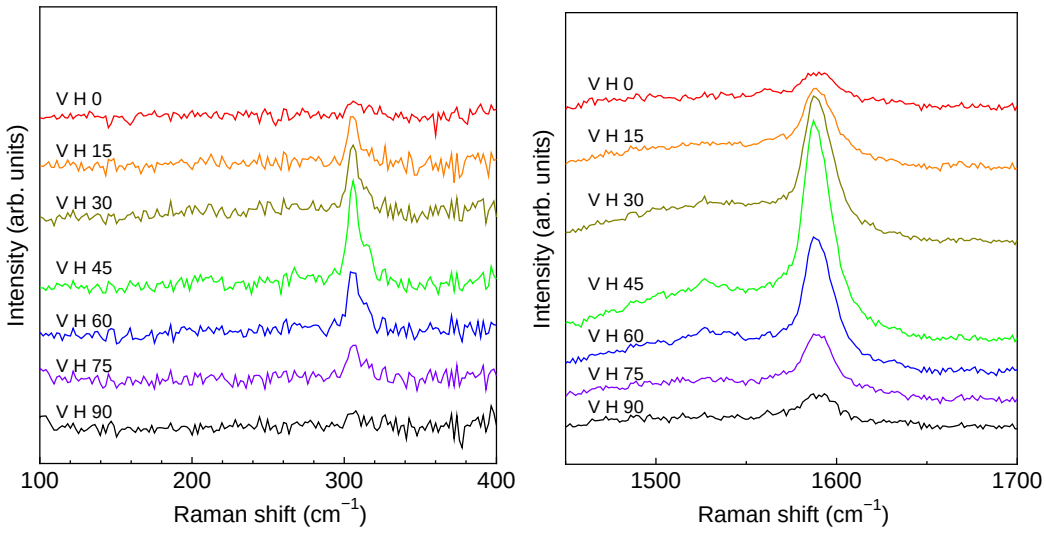

(a) RBM (b) G-band

Figure 5.4: Raman spectra of the stretched CoMoCat-PVA film in the VH configuration with the incident polarization changing from 0° (along alignment direction) to 90° (perpendicular to the alignment direction).

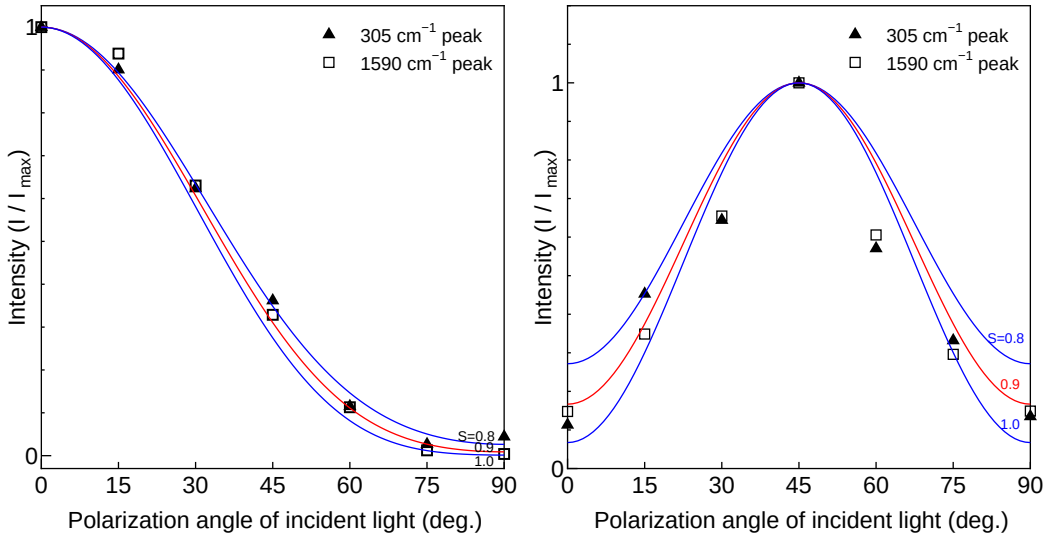

(a) in VV configuration

(b) in VH configuration

Figure 5.5: Normalized RBM Peak intensity changes as the function of incident light polarization in (a)VV and (b)VH configuration

To identify the feature explicitly, we plot the peak intensity at 305 cm^{-1} as the function of polarization angle as shown in Fig. 5.5. The normalized peak intensity agrees well with the calculated curve considering parallel excitation and gives high alignment of order parameter about 0.9 in both VV and VH configuration. Moreover, the normalized intensity of G^+ peak at 1590 cm^{-1} is plotted in the same figure and shows very similar trend as 305 cm^{-1} peak.

All the optical absorptions and Raman spectra shows preemient alignment of CoMoCat-SWNTs in the stretched PVA film, which provides an advantageous sample to investigate the optical polarization dependence of SWNTs. Under 488 nm excitaion, all the Raman peaks behave as parallel excitation and no perpendicularly-polarized Raman signal is observed in this sample.

Chapter 6

Summary

This research conducted during the master course mainly investigated the polarization dependence in Raman spectroscopy of vertically aligned single-walled carbon nanotubes (VA-SWNTs). Theoretical calculation models for each observable Raman mode were established based on selection rules for the first-order Raman scattering of SWNTs. The dipole approximation method was used in the calculation, which appeared to be a universal means for discussing optical absorption/scattering in SWNTs.

The polarized Raman measurements were carried out with two configurations, VV and VH, to analyze both incident and scattered light. The tangential G-band was decomposed into six peaks to study the A, E_1 and E_2 modes from different geometry settings, and the A vibration mode was found to be dominant in the Raman spectra. The G^+ peak frequency shift indicates the temperature change of the sample due to the different absorption ratios at each polarization angle, which is used to discuss the temperature effect on G-band and radial breathing mode (RBM) peaks.

Two polarization dependences of RBM peaks were found in VV Raman spectra. The {160 and 203 cm^{-1}} group peaks behave as an antenna, where absorption is strongest (weakest) when incident light is parallel (perpendicular) to the tube axis. The other group of {145, 180, 245, and 256 cm^{-1}} peaks behave oppositely. This anomaly was previously attributed to perpendicularly-polarized excitation with resonance of $E_{\mu\mu\pm1}$ (μ denotes the cutting line index), since the dominant 180 cm^{-1} could not be assigned using earlier theoretical Kataura plot. However, the 180 cm^{-1} peak was recently found to be composed of four small peaks in high resolution Raman spectroscopy, and they can be well assigned in a revised experimental Kataura plot.

By carefully decomposing the RBM peaks into Lorentzian curves and plotting the intensity dependence as a function of polarization angle, the $\{203\,\mathrm{cm}^{-1}\}$ group peaks fit well with the parallel excitation assumption, while the $\{180\,\mathrm{cm}^{-1}\}$ group peaks deviate by 40% from the perpendicularly-polarized assumption. Furthermore, after correcting for temperature effects to the Raman spectra, the $\{180\,\mathrm{cm}^{-1}\}$ group peak intensities become nearly constant for all polarization angles. Therefore, a new hypothesis is proposed that the RBM anomoly is due to the parallel excitation from suspended SWNTs with the VA-SWNT forest, which have been observed by SEM.

Moreover, a technique of aligning the SWNTs was developed by stretching the SWNT-dispersed PVA film, where the alignment with a order parameter about 0.9 was achieved. The polarized Raman spectroscopy from this aligned sample revealed that RBM and G-band peaks all behave consistently with the antenna effect, and no perpendicularly-polarized peaks were observed. This supports the hypothesis mentioned above. More extensive investigations on optical polarization dependence of SWNTs are expected by using this promising aligned SWNTs sample.

Acknowledgments

First and foremost, I feel very grateful to the Panasonic scholarship, which always supported me during my master course both materially and mentally.

In these two-year study in Japan, many people generously helped me and I would like to thank them all. The people I feel like to appreciate most is Professor Maruyama, who mentored and encouraged me to be a conscientious researcher: alway keeping curiosity to the unknown world and never stopping pursuing truth. I am gratful to Dr. Miyauchi for teaching me the skills and knowledges of spectroscopy, which opened my eye to a whole new world of CNTs. I will always remember his description of "doing experiment is like cooking". I would like to thank Erik, who always generously helped me and carefully taught many new things. He let me know one should always pursuing perfection. I would like to thank Xiang Rong and Dr. Murakami, who gave me many important suggestions and instructions during the research. I am also grateful to Dr. Shiomi and Dr. Chiashi for valuable discussions, as well as Ogura san, Ookawa san, Izu san...Thank you all for the kind help.

I also like to thank the people I have collaborated with, Professor Noda, Hasegawa san, Sugime san, Shiratori san from the department of chemical system engineering, for the kind discussions and suggestions.

At last I sincerely show my deep thank to my family for selflessly supporting me all the time.

Bibliography

[1] H. W. Kroto, J. R. Heath, S. C. O'Brien, R. F. Curl, R. E. Smalley, C_{60}: Buckminsterfullerene, Nature 318 (1985) 162–163.

[2] S. Iijima, Helical microtubules of graphitic carbon, Nature 354 (1991) 56–58.

[3] S. Iijima, T. Ichihashi, Single-shell carbon nanotubes of 1-nm diameter, Nature 363 (1993) 603–605.

[4] R. Saito, G. Dresselhaus, M. S. Dresselhaus, Physical Properties of Carbon Nanotubes, Imperial College Press, London, 1998.

[5] M. S. Dresselhaus, G. Dresselhaus, P. Avouris, Carbon Nanotubes: Synthesis, Structure, Properties, and Applications, Vol. 80, Springer, Berlin, 2001.

[6] S. Reich, C. Thomsen, J. Maultzsch, Carbon Nanotubes: Basic Concepts and Physical Properties, Wiley, 2004.

[7] S. Chiashi, Single-walled carbon nanotube synthesis in an environmental AFM and in situ Raman spectroscopy (in Japanese), Ph.D. thesis, The University of Tokyo (2005).

[8] K. Sato, R. Saito, J. Jiang, G. Dresselhaus, M. S. Dresselhaus, Discontinuity in the family pattern of single wall carbon nanotubes, Phys. Rev. B 76 (2007) 195446.

[9] A. Jorio, G. Dresselhaus, M. S. Dresselhaus, Carbon Nanotubes, Springer, 2008.

[10] P. T. Araujo, S. K. Doorn, S. Kilina, S. Tretiak, E. Einarsson, S. Maruyama, H. Chacham, M. A. Pimenta, A. Jorio, Third and fourth optical transitions in semiconducting carbon nanotubes, Phys. Rev. Lett. 98 (2007) 067401.

[11] A. Jorio, A. G. S. Filho, V. W. Brar, S. A. K., M. S. Ünlü, B. B. Goldberg, A. Righi, J. H. Hafner, C. Lieber, R. Saito, G. Dresselhaus, M. S. Dresselhaus, Polarized resonant raman study of isolated single-wall carbon nanotubes: Symmetry section rules, dipolar and multipolar antenna effects, Phys. Rev. B 65 (2002) 121402.

[12] A. Jorio, M. A. Pimenta, A. G. S. Filho, G. G. Samsonidze, A. K. Swan, M. S. Ünlü, B. B. Goldberg, R. Saito, G. Dresselhaus, M. S. Dresselhaus, Resonance raman spectra of carbon nanotubes by cross-polarized light, Phys. Rev. Lett. 90 (2003) 14.

[13] A. Jorio, M. A. Pimenta, A. G. S. Filho, R. Saito, G. Dresselhaus, M. S. Dresselhaus, Characterizing carbon nanotube samples with resonance raman scattering, New J. Phys. 5 (2003) 139.1–139.17.

[14] M. S. Dresselhaus, G. Dresselhaus, R. Saito, A. Jorio, Raman spectroscopy of carbon nanotubes, Phys. Rep. 409 (2005) 47–99.

[15] A. Jorio, G. Dresselhaus, M. S. Dresselhaus, M. Souza, M. S. S. Dantas, M. A. Pimenta, A. M. Rao, R. Saito, C. Liu, H. M. Cheng, Polarized raman study of single-wall semiconducting carbon nanotubes, Phys. Rev. Lett. 85 (2000) 2617–2620.

[16] A. Grüneis, R. Saito, J. Jiang, G. G. Samsonidze, M. A. Pimenta, A. Jorio, A. G. S. Filho, G. Dresselhaus, M. S. Dresselhaus, Resonant Raman spectra of carbon nanotube bundles observed by perpendicularly polarized light, Chem. Phys. Lett. 387 (2004) 301–306.

[17] G. G. Samsonidze, R. Saito, A. Jorio, M. A. Pimenta, A. G. S. Filho, A. Grüneis, G. Dresselhaus, M. S. Dresselhaus, The concept of cutting lines in carbon nanotube science, J. Nanosci. Nanotechnol. 3 (2003) 431–458.

[18] Y. Murakami, CVD growth of single-walled carbon nanotubes and their anisotropic optical properties, Ph.D. thesis, The University of Tokyo (2005).
URL `www.photon.t.u-tokyo.ac.jp/thesis/2005/2005murakami.pdf`

[19] Y. Miyauchi, Ph.D. thesis, the University of Tokyo (2006).

[20] Y. Murakami, S. Chiashi, E. Einarsson, S. Maruyama, Polarization dependence of resonant Raman scatterings from vertically aligned SWNT films, Phys. Rev. B 71 (2005) 085403.

[21] Y. Murakami, E. Einarsson, T. Edamura, S. Maruyama, Polarization dependence of the optical absorption of single-walled carbon nanotubes, Phys. Rev. Lett. 94 (2005) 087402.

[22] C. Kramberger, H. Shiozawa, H. Rauf, A. Grüneis, M. H. Rümmeli, T. Pichler, B. Buchner, D. Batchelor, E. Einarsson, S. Maruyama, Anisotropy in the x-ray absorption of vertically aligned single wall carbon nanotubes, phys. stat. sol. (b) 244-11 (2007) 3978–3981.

[23] C. Fantini, A. Jorio, M. Souza, M. S. Strano, M. S. Dresselhaus, M. A. Pimenta, Optical transition energies for carbon nanotubes from resonant raman spectroscopy: Enviromen and tempearature effects, Phys. Rev. Lett. 93 (2004) 14.

[24] G. S. Duesberg, I. Loa, M. Burghard, K. Syassen, S. Roth, Polarized raman spectroscopy on isolated single-wall carbon nanotubes, Phys. Rev. Lett. 85 (2000) 5436.

[25] S. Chiashi, Y. Murakami, Y. Miyauchi, S. Maruyama, Tempearature dependence of raman scattering from single-walled carbon nanotubes: Undefined radial breathing mode peaks at high tempearatures, Jpn. J. Appl. Phys. 47 (2008) 2010–2015.

[26] A. G. Rozhin, Y. Sakakibara, M. Tokumoto, H. Kataura, Y. Achiba, Near-infrared nonlinear optical properties of single-wall carbon nanotubes embedded in polymer film, Thin Solid Films 464-465 (2004) 368–372.

[27] A. G. Rozhin, Y. Sakakibara, H. Kataura, S. Matsuzaki, K. Ishida, Y. Achiba, M. Tokumoto, Anisotropic saturable absorption of single-wall carbon nanotubes aligned in polyvinyl alcohol, Chem. Phys. Lett. 405 (2005) 288–293.

[28] M. Ichida, S. Mizuno, H. Kataura, Y. Achiba, A. Nakamura, Anisotropic optical properties of mechanically aligned single-walled carbon nanotubes in polymer, Appl. Phys. A 78 (2004) 1117–1120.

[29] A. Jorio, A. P. Santos, H. B. Ribeiro, C. Fantini, M. Souza, J. P. Vieira, C. A. Furtado, J. Jiang, R. Saito, L. Balzano, D. Resasco, M. A. Pimenta, Quantifying carbon-nanotube species with resonance raman scattering, Phys. Rev. B 72 (2005) 075207.